Journal of Iberian Geology (2022) 48:461–486
https://doi.org/10.1007/s41513-022-00201-7

RESEARCH PAPER

Petrogenesis and geodynamic implications of Oligocene A-type granite in the Guadalcazar area, San Luis Potosi, central Mexico

Sanjeet K. Verma[1] · Darío Torres-Sánchez[2] · Diego A. de León Hernández[1] · Elson P. Oliveira[3] · Karla R. Hernández-Martínez[1] · Sonia A. Torres-Sánchez[4] · José R. Torres Hernández[5] · Juan A. Moreno[6] · Mayank Shukla[1] · Vivek P. Malviya[7]

Received: 21 April 2022 / Accepted: 8 November 2022 / Published online: 28 November 2022

Abstract

The Guadalcazar is located in the Mesa Central (MC) province, which is mainly composed of granitic rocks and is known for its metallogenetic. The granitic rocks contain complex Sn-Hg-Ag-F mineralization and were emplaced during Eocene to Oligocene. However, the source, origin, and evolution of magma and the tectonic setting of this magmatic area have never been explained. In this study, we have conducted petrology, whole-rock geochemistry, and U–Pb zircon geochronology on granitic rocks from the Guadalcazar to constrain the petrogenesis and tectonic environment. LA-ICP-SF-MS zircon U–Pb dating shows that the Guadalcazar granite was emplaced ca. 31 Ma. These rocks are characterized by high (SiO_2) contents (64–75 wt%), low CaO (0.28–1.78 wt%), with relatively high $(FeO^t)_{adj}/(FeO^t + MgO)$ values ranging from 0.90 to 0.98. The geochemical diagrams of SiO_2 vs $[(FeO^t)/(FeO^t + MgO)]$ and SiO_2 vs $[(Na_2O + K_2O) - CaO]$ show the ferroan and mostly alkali-calcic nature of these rocks. The granite shows an A_2-type affinity and is strongly peraluminous, with ASI (molar $Al_2O_3/[CaO + Na_2O + K_2O]$) values of 1.13 to 2.60. These granitic rocks are characterized by enrichments in rare earth elements (REE) and high field strength elements (HFSE), and depletion in Ba, Nb, Sr, Ti, and Eu. These features suggest that these A-type granites were derived from the metasedimentary rocks and evolved through extensive fractional crystallization. The multidimensional discrimination diagrams showed a continental rift or within-plate setting. By combining previous and new data, we proposed a new magmatic evolution model that supports an extension during ca. 34–28 Ma in the Guadalcazar, central Mexico.

Keywords Geochemistry · Granite · Petrogenesis · Guadalcazar · Mexico

Resumen

La región de Guadalcazar situada en la provincia de Mesa Central (MC), está formada principalmente por rocas graníticas y es conocida por su importancia metalogenética. Las rocas graníticas presentan mineralizaciones de Sn-Hg-Ag-F y se emplazaron durante el Eoceno-Oligoceno. Sin embargo, la fuente, origen y evolución de estos magmas, así como el contexto tectónico de esta región magmática nunca han sido explicados. En este trabajo se han realizado estudios petrográficos, de geoquímica de roca total y geocronología de U-Pb en circón en rocas graníticas de Guadalcazar con el fin de entender su

✉ Sanjeet K. Verma
sanjeet.verma@ipicyt.edu.mx; sanjeet_vrm@yahoo.com

[1] División de Geociencias Aplicadas, Instituto Potosino de Investigación Científica y Tecnológica (IPICYT), Camino a la Presa San José 2055, 78216 San Luis Potosí, Mexico

[2] Instituto de Geofísica, Unidad Michoacán, Universidad Nacional Autónoma de Mexico, Antigua Carretera a Pátzcuaro 8701, 58190 Morelia, Michoacán, Mexico

[3] Department of Geology and Natural Resources, Institute of Geosciences, University of Campinas-UNICAMP, PO Box 6152, Campinas, SP 1303-970, Brazil

[4] Facultad de Ingeniería, Área de Geología, Universidad Autónoma de San Luis Potosí, Manuel Nava No. 5 Zona Universitaria, 78240 San Luis Potosí, Mexico

[5] Instituto de Geología, Universidad Autónoma de San Luis Potosí, Manuel Nava No. 5 Zona Universitaria, 78240 San Luis Potosí, Mexico

[6] Departamento de Mineralogía y Petrología, Facultad de Ciencias Geológicas, Universidad Complutense (UCM), 28040 Madrid, Spain

[7] 24E Mayur Residency Ext., Indra Nagar, Lucknow 226015, India

petrogénesis y el ambiente tectónico. La datación por U-Pb en circón mediante LA-ICP-SF-MS indica que el granito Guadalcazar se emplazó hace ca. 31 Ma. Estas rocas se caracterizan por presentar altos contenidos de SiO_2 (64–75 % en peso), bajos contenidos de CaO (0.28–1.78 % en peso), y valores elevados de la razón $(FeO^t)_{adj}/(FeO^t+MgO)$ que varían entre 0.90 y 0.98. Las rocas estudiadas presentan un carácter ferroso y una naturaleza principalmente álcali-cálcica en los diagramas SiO_2 vs $[(FeO^t)/(FeO^t+MgO)]$ y SiO_2 vs $[(Na_2O+K_2O)-CaO]$. Este granito muestra afinidad de tipo A_2 y es fuertemente peraluminoso con valores del índice saturación en alúmina ($ISA = Al_2O_3/[CaO + Na_2O + K_2O]$ en moles) que varían entre 1.13 y 2.6. Estos granitos se caracterizan por un enriquecimiento en tierras raras (REE) y en elementos de alto potencial iónico (HFSE) y empobrecimiento en Ba, Nb, Sr, Ti y Eu. Estas características sugieren que estos granitos de tipo A derivan de rocas metasedimentarias y evolucionaron por una extensa cristalización fraccionada. Los diagramas de discriminación multidimensional indican un contexto de rift continental o intraplaca. Combinando datos nuevos y previos, se propone un nuevo modelo magmático que sugiere/apoya un ambiente extensional hace ca. 34–28 Ma en la zona de Guadalcazar, región central de México.

Palabras clave Geoquímica · Granito · Petrogénesis · Guadalcazar · México

1 Introduction

Granitic rocks are the main components of continental crust and are widely evolved as the end-products of growth of the Earth's continental crust (Castro, 2014; Kemp & Hawkesworth, 2003). During continental crust development, the granitic rocks display great diversity in their origin, source, evolution, and geodynamic environments of formation (Barbarin, 1999). Determining the origin and emplacement of the granitic rocks are thus crucial for understanding continental crustal growth and crustal evolution (e.g., Moreno et al., 2014, 2017; Singh et al., 2019, 2021; Verma, et al., 2016). In central Mexico, the Mesa Central (MC) province is situated. The MC has been described as an elevated plateau that covers the central-northern Mexico part and is mainly bounded by the Sierra Madre Oriental (SMOr) and the Sierra Madre Occidental (SMOc) (Fig. 1; Nieto-Samaniego et al., 2007; Torres-Sánchez et al., 2019, 2020). In the MC, the granitic rocks mainly exist in the four localities (1) Sierra de Catorce (2) Sierra del Fraile (3) Peñón Blanco, which are located in the central west of MC (Pinto-Linares et al. 2008; Mascuñano et al., 2013; Huerta-González, 2017; Siesgesmund et al., 2018; Silva-Romo, 1996; Nieto-Samaniego et al., 2005, 2020; Aranda-Gómez et al., 2007; Tristán-González et al., 2015; Cuéllar-Cárdenas et al., 2012), and (4) the Guadalcazar Granite at the central-eastern portion of the MC (Chryssoulis & Wilkinson, 1983; Tuta et al., 1988; Torres-Jurado, 2019, Díaz-Bravo et al., 2022). Several studies have been performed on the characterization and origin of the Sierra de Catorce, Sierra del Fraile, and Peñón Blanco (Cuéllar-Cárdenas et al., 2012; Siesgesmund et al., 2018; Díaz-Bravo et al., 2022) that play an important role to understand the formation of Mexican crust and its mineralization. However, such studies from the Guadalcazar granites are still not constrained, which holds clues on the composition and classification of these granites that allow inferences on their origin and related tectonic environment. In this sense, geochemical studies and petrogenetic interpretations can be important tools to understand the whole scenario. Therefore, here we present new major and trace element geochemical data, including the rare-earth elements (REE), as well as new U–Pb zircon dating to discuss the origin, source, evolution, and tectonic implications of the Guadalcazar granites.

2 Geological background

The southern region of the MC is mainly composed of widespread Cenozoic fault systems such as: (a) the NW–SE trending El Bajío (EB) in the south; (b) the Taxco-San Miguel de Allende (TSM) in the west; and (c) the San Luis-Tepehuanes (SLT) extending within the MC (Nieto-Samaniego et al., 2007). In addition, the MC is divided into two main regions: (i) the northern region, which is characterized by advanced stages of erosion, alluvial-lacustrine basin development and a few magmatic rocks of Cenozoic ages; (ii) the southern region, which is covered by Paleogene–Neogene volcanic rocks and cross-cut by several normal faults (Fig. 1; Nieto-Samaniego et al., 2007; Torres-Sánchez et al., 2019, 2020). Due to the fault systems, the volcanic activities in the MC were generated in an extensional setting (Torres-Sánchez et al., 2020). This region is also underpinned by a Mesozoic basement comprising marine calcareous rocks of the SMOr, and volcanic-flysch sequences of the Sierra de Guanajuato Complex (Centeno-García, 2017; Orozco-Esquivel et al., 2002). The plutonic bodies exist in the MC are characterized by porphyritic stocks, dykes and extensive sub-volcanic rocks. Their ages range from the Late Cretaceous to early Oligocene. The MC shows similar ages to plutonic rocks of the SMOr that range from 83 to 32 Ma (U–Pb) and from 88 to 32 Ma (K–Ar) (Castro-Reino 2004; Velasco-Tapia et al., 2011; González-Guzmán 2012). During the Late Cretaceous-Paleogene, a less amount of post-Laramide granites bodies emplaced within the southern region of

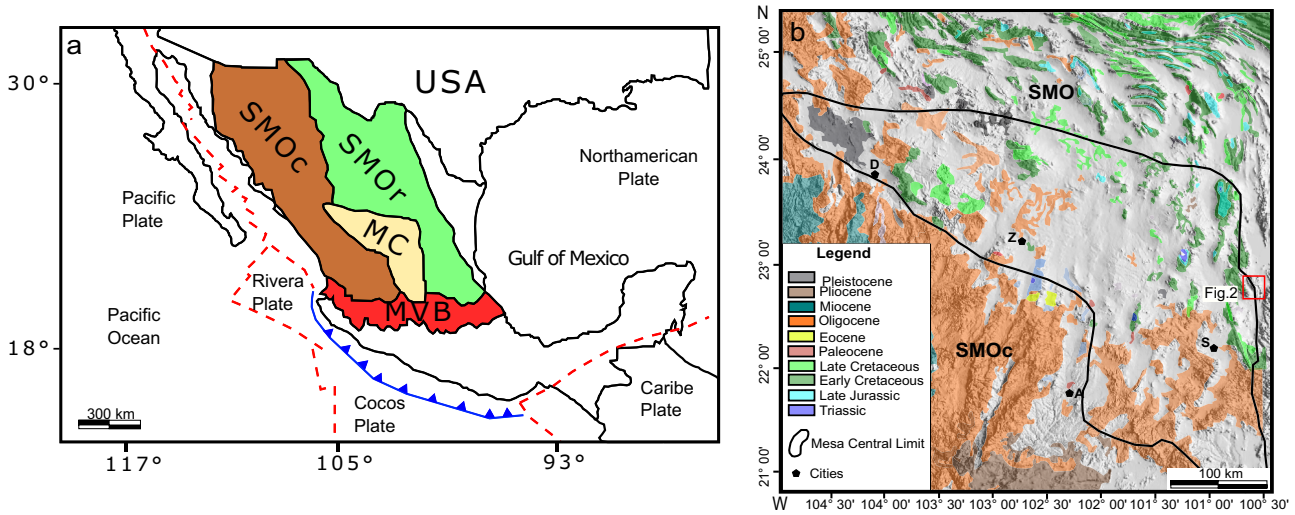

Fig. 1 **a** Present-day regional tectonic map of Mexico with subdivisions of the main physiographic provinces (modified after Nieto-Samaniego et al., 2007; Verma et al., 2020); **b** Simplified geological map of the MC province (modified after Nieto-Samaniego et al., 2007). *MC* Mesa Central, *SMOc* Sierra Madre Occidental, *SMOr* Sierra Madre Oriental, *MVB* Mexican Volcanic Belt

the MC (Angeles-Moreno et al., 2017) that extended along the Pacific margin and extensional magmatism of the SMOc, which know as a silicic large igneous province of the late Eocene-early Miocene. The MC overlaps temporarily two magmatic events of SMOc such as (1) the origin of intermediate rocks by extensional magmatism and growth of various plutons during the Eocene (50–40 Ma; Ferrari et al., 2018) and (2) ignimbrite magmatism flare-up of the SMOc during Eocene to Oligocene (38–28 Ma; Ferrari et al., 2018).

The Guadalcazar granite is located within the central zone of the MC (Figs. 1 and 2a, b) 90 km northeast of the San Luis Potosi. The mountain corresponds to the Valles-San Luis Potosí Platform, which began to form at the end of the Paleozoic, and was later exposed to the sedimentary rocks (Aranda-Gómez et al., 2000). The sedimentary rocks were folded and deformed during the Late Cretaceous to the middle Eocene. During the deformation of the sedimentary rocks, several plutonic bodies were emplaced, having the composition of felsic to intermediate rocks. The Guadalcazar granite is part of the plutonic rocks (Aranda-Gómez et al., 2000; Salas, 1975). The granite is mainly characterized by a porphyry stock, which is roughly circular in outcrop with a diameter of 2–3 km (Chryssoulis & Wilkinson, 1983; Tuta et al., 1988). The granite body displays an intrusive contact with platform carbonates and sandstone-limestone sequences (Guaxcamá, El Abra, and Cárdenas Formation; Fig. 3) on all sides with an exception to the northeast contact, where alluvium deposits cover the granite (Chryssoulis & Wilkinson, 1983; Foshag & Fries, 1942). Numerous hydrothermal alterations and mineralization (mercury, silver, and tin) exist along the contact of the Guadalcazar intrusive body (Chryssoulis & Rankin, 1988). Fries and Schmitter (1948); Chryssoulis and Wilkinson (1983); Chryssoulis and Rankin (1988) proposed a series of decrepitating experiments on fluid inclusion in quartz from the Guadalcazar granite to understand metallogeny. Aranda-Gómez et al. (2000) have discussed the structural and morphological features, which are mainly related to the modification of Laramide Orogeny fold system that affects the northeastern-central part of Mexico including the Valles-San Luis Potosí. Other workers (Chryssoulis & Rankin, 1988; Tuta et al., 1988) reported Ar–Ar and K–Ar ages of (28.6–28.3 Ma) and (34.7–30.7 Ma) respectively, for the Guadalcazar granite and suggesting (Silver, Lead, Zinc, and Tin) hydrothermal mineralization. Recently, Díaz-Bravo et al. (2022) provided an additional $^{238}U/^{206}Pb$ age of 31.45 ± 0.17 Ma for one granite. In addition, the Guadalcazar granite intrusive body cuts a thick calcareous breccia (El Realejo Formation; Fig. 3) and deposits of conglomerate with breccia clast (El Muerto Formation; Fig. 3). Aranda-Gómez et al. (2000) reported that the Guadalcazar granite displays fold axes of the host rock that follow a regional trend of ~ 320° and their traces are relatively straight. Towards the center of the Guadalcazar the fold axes from host rocks become concave near the mid-Tertiary stock and collapse breccia (Aranda-Gómez et al., 2000).

3 Sampling and analytical methods

A total of 25 fresh samples were collected through the whole plutonic body. Alteration areas, deformation and veins were avoided during sampling, and only fresh samples were used for geochemical analysis. Sampling coordinates are

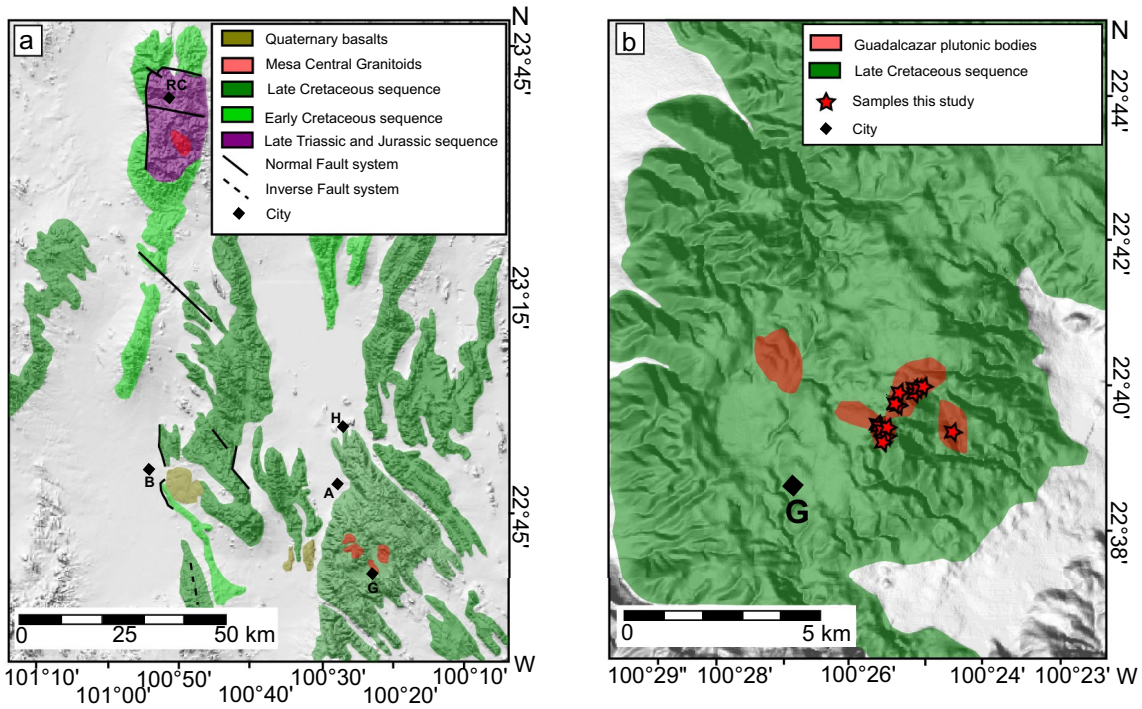

Fig. 2 **a** Geological map of the margin of the Mesa Central (MC) province and the Valle-San Luis Potosí Platform (VSLP; modified after Aranda-Gómez et al., 2000); **b** Geological map of the Guadalcazar area, showing the space distribution of the granite body. *RC* Real de Catorce, *B* Bustamante, *A* Los Amoles, *H* El Huizache, *G* Guadalcazar

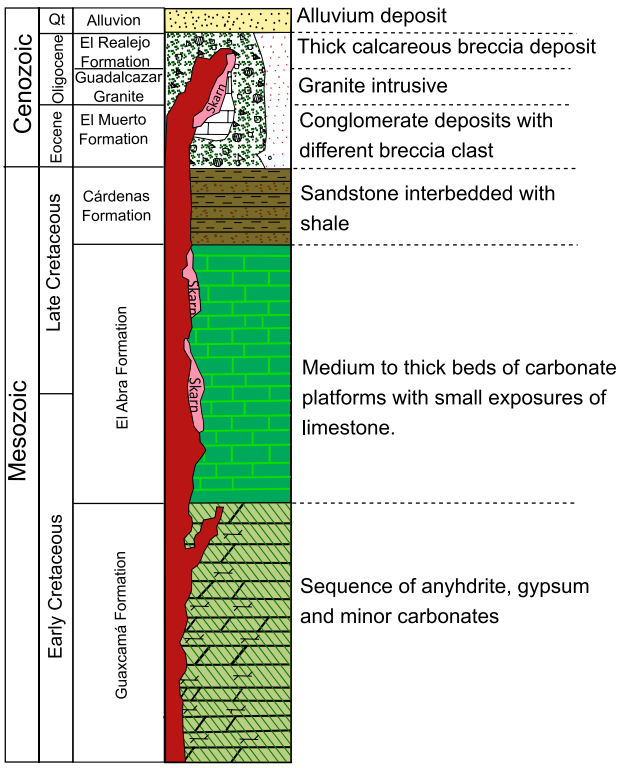

Fig. 3 Schematic stratigraphic column for the Guadalcazar area

presented in Tables 1 and 2. The modal composition of 5 samples was determined by point-counting on a thin section using a Leica petrographic microscope and a PELCON Automatic point counter. In order to obtain a representative mode, approximately 1000 points per sample were counted. The data are reported in Table 1.

The major elements for 25 samples were determined by a wavelength dispersive X-ray fluorescence (WD-XRF) spectrometer Rigaku ZSX Primus II at Institute of Scientific and Technological Research of San Luis Potosi, IPICYT (San Luis Potosí, Mexico). Analytical procedures, accuracy and precision are given by Ruiz-Mendoza et al. (2021), Verma et al., (2018, 2019). The computer program Major element Concentration and its Uncertainty from X-ray fluorescence (MECUX) were used to obtain the concentrations of the samples. Trace and rare earth elements concentrations were determined by Inductively Coupled Plasma Mass Spectrometry (ICP-MS) in ACTLABS (Vancouver, Canada) using the *4B2-Std* method. The precision (standard deviation) estimates were < 2–3% for trace elements, and < 1–2% for rare earth elements (REEs). The analytical precision is based on geochemical reference material SY-4, BIR-1a, ZW-C, OREAS 101b, NCS DC86318, USZ 42-2006, and SARM 3.

Geochronological information was determined by selecting one representative rock sample (GA-03) for zircon U–Pb dating. About 5–6 kg sample was crushed with a jaw crusher and powdered to approximately 300 µm using a disc ball

Table 1 Petrographic information of the Sierra de Guadalcazar plutonic rocks

Sample	QAFP diagram classification	Lat (N)°	Long (W)°	Texture	Phenocrysts						
					Qz	FldK	Plg	Bt	Msc	Zr	Op
GA-04	Granite	22° 39′ 59"	100° 24′ 58"	P	37.4	48	5.8	7.3	–	0.9	0.6
GA-08	Granite	22° 39′ 55"	100° 25′ 14"	P	39	39.6	6.6	10	1.2	0.8	2.7
GA-12	Alkali-feldspar granite	22° 39′ 46"	100° 25′ 18"	P	44.9	50	0.3	–	4.3	0.5	–
GA-16	Alkali-feldspar granite	22° 39′ 26"	100° 25′ 31"	P	41.7	48.2	3.4	4	1.4	0.2	1.1

Modal data are presented in percentage

Texture: *P* phaneritic, *Plg* plagioclase, *Qz* quartz, *FldK* potassium feldspar, *Bt* biotite, *Op* opaque minerals

mill. Heavy mineral concentrates were obtained by panning and were subsequently purified using Nd magnets, a Frantz magnetic separator and methylene iodide; after that obtained zircon grains were mounted in 1 in. round epoxy mounts resin, polished using the diamond paste, and cleaned using 10% v/v HNO_3 followed by de-ionized water. Zircon grains were studied by cathodoluminescence imaging (CL) to reveal their internal structures and to help select optimum spot locations. Zircon U–Pb dating was obtained using an ICP-MS element XR (Thermo Scientific) at the IG-UNICAMP, Brazil (for more detail: see Singh et al., 2019, 2021; Verma et al., 2016). U-Th-Pb ratios and absolute abundances were determined relative to the standard zircon 91,500 (Wiedenbeck et al., 1995). Data were reduced off-line using lolite software (version 2.5) following the method described by Paton et al. (2010). Peixe zircon standard (ID-TIMS age of 564 ± 4 Ma; Dickson & Gehrels, 2003) was used to monitor the quality of the reduction procedures. Data are reported with 2 sigma uncertainties and are plotted using the software ISOPLOT 3.75 (Ludwig, 2012).

4 Results

4.1 Petrography

The microscopic characteristics and main mineral assemblages of the Guadalcazar granite samples are summarized in Table 1 and Fig. 4a–f. Petrographic classification from the Guadalcazar samples has been based on the Quartz, Alkali feldspar, and Plagioclase (QAP) diagram (Le Maitre et al., 2002). In the QAP diagram the studied samples plot as alkali-feldspar granites, with the exception of two samples plot as syenogranites but close to the limit with the alkali-feldspar granites (Fig. 4a). Samples plotted in the granite field (Fig. 4a) display medium to coarse grains (Fig. 4b, c). The main mineral assemblage of the granite samples consists of phenocrysts of quartz (37–39%; Table 1); euhedral to subhedral phenocrysts of K-feldspar (39–48%) with diameters ranges of 0.5–1 mm; subhedral phenocryst of plagioclase (5.8–6%) with diameters of 0.3–0.8 mm (Fig. 4b, c), some of these crystals display sieved textures. In addition, the granite samples (GA-04 and GA-08) display subhedral phenocrysts of biotite (7–10%), and opaque minerals. Furthermore, it can be observed that biotite in granites samples shows pleochroic haloes probably of zircon inclusion (sample GA-04; Fig. 4d).

On the other hand, the samples plotted in the alkali-feldspar granite field (Fig. 4a) display few textures difference from granite samples. The main difference in texture between these two kinds of samples is the coarse grains observed in the alkali feldspar granite samples (GA-12 and GA-16; Fig. 4e, f). The main mineral assemblage of this samples are: (i) phenocrysts of quartz (41–44%; Table 1); (ii) euhedral-subhedral phenocrysts of K-feldspar (48–50%) with variable diameters of 0.2 to 1 mm; (iii) euhedral to subhedral phenocrysts of plagioclase (0.3–3.4%) with diameters of 0.2–0.5 mm (Fig. 4e, f); and (iv) biotite (~4%) and muscovite (1.4–4.3%) crystals with diameters ranges of 0.1–0.3 mm. In contrast, the alkali-feldspar granite samples have zircons as the main accessory (Table 1) and a scarce presence of pleochroic haloes.

4.2 Major and trace element concentration

The major element compositions of 25 samples are summarized in Table 2. Fe-oxidation adjustment was obtained by IgRoCS program (Verma & Rivera-Gómez, 2013) under the Middlemost (1989) option. The major-element composition after IgRoCS processing is recognized by the subscript adj added to each major-oxide name. Based on TAS diagram (Le Bas et al., 1986; Fig. 5a), the Guadalcazar granitic samples were divided into three groups: granite, syeno-granite and granodiorite. The granite samples are characterized by $(SiO_2)_{adj}$ values of 69.10–75.33 wt%, $(Al_2O_3)_{adj}$ of 14.88–21.68 wt%, $(CaO_2)_{adj}$ of 0.28–1.79 wt% and $(K_2O)_{adj}$ of 4.24–6.17 wt% (Table 2). The granite samples display A/NK and A/CNK ratios values of 1.65–2.99 and 1.49–2.88 respectively, indicating a peraluminous tendency (Fig. 5b). On the other hand, the syeno-granite samples show $SiO_2)_{adj}$ values of 64.22–68.68 wt%, $(Al_2O_3)_{adj}$ of 18.66–25.70 wt%, $(CaO_2)_{adj}$ of 0.29–1.18 wt% and $(K_2O)_{adj}$ of 5.79–8.17 wt% (Table 2). Similar to the granite samples, the syeno-granite rocks display a peraluminous trend (Fig. 5b). The

Table 2 Representative whole rock compositions of granitic rocks from the Guadalcazar intrusive body, San Luis Potosí, Mexico

Sample	GA-01	GA-02	GA-03	GA-04	GA-05	GA-06	GA-07	GA-08	GA-09
Rock (TAS)	Granite	Syeno-granite	Granite	Syeno-granite	Syeno-granite	Granite	Syeno-granite	Syeno-granite	Syeno-granite
Long. (°W)	22° 39′ 56"	22° 39′ 58"	22° 39′ 59"	22° 39′ 59"	22° 40′ 01"	22° 39′ 59"	22° 39′ 58"	22° 39′ 55"	22° 39′ 48"
Lat. (°N)	100° 25′ 01"	100° 24′ 58"	100° 24′ 58"	100° 24′ 58"	100° 24′ 54"	100° 25′ 01"	100° 25′ 01"	100° 25′ 14"	100° 25′ 18"
Major elements									
SiO_2	72.158	68.192	69.828	65.257	65.439	68.673	63.84	67.608	65.312
TiO_2	0.117	0.145	0.159	0.134	0.172	0.087	0.081	0.139	0.097
Al_2O_3	14.783	18.526	17.174	22.455	22.469	20.35	25.552	20.818	24.346
$Fe_2O_3^t$	2.397	1.901	2.422	0.801	2.2	1.284	1.033	1.794	1.498
MnO	0.127	0.128	0.101	0.063	0.112	0.046	0.056	0.06	0.058
MgO	0.038	0.039	0.041	0.039	0.039	0.038	0.038	0.038	0.038
CaO	0.922	1.169	1.038	0.816	0.691	0.666	0.355	0.748	0.291
Na_2O	3.059	2.545	2.602	1.759	2.325	2.606	2.141	2.328	1.95
K_2O	5.893	6.751	6.003	8.126	5.79	5.692	6.354	5.881	5.745
P_2O_5	0.018	0.03	0.02	0.031	0.034	0.022	0.032	0.029	0.012
LOI	0.016	0.085	0.121	0.032	0.213	0.053	0.034	0.069	0.136
Sum	99.53	99.51	99.51	99.51	99.48	99.52	99.52	99.51	99.48
Adjusted value									
$(SiO_2)_{adj}$	72.633	68.676	70.376	65.634	66.021	69.105	64.218	68.072	65.810
$(TiO_2)_{adj}$	0.118	0.146	0.160	0.135	0.174	0.088	0.081	0.140	0.098
$(Al_2O_3)_{adj}$	14.880	18.658	17.309	22.585	22.669	20.478	25.703	20.961	24.532
$(Fe_2O_3)_{adj}$	0.749	0.594	0.757	0.250	0.689	0.401	0.322	0.560	0.468
$(FeO)_{adj}$	1.497	1.188	1.515	0.500	1.377	0.802	0.645	1.121	0.937
$(MnO)_{adj}$	0.128	0.129	0.102	0.063	0.113	0.046	0.056	0.060	0.058
$(MgO)_{adj}$	0.038	0.039	0.041	0.039	0.039	0.038	0.038	0.038	0.038
$(CaO)_{adj}$	0.928	1.177	1.046	0.821	0.697	0.670	0.357	0.753	0.293
$(Na_2O)_{adj}$	3.079	2.563	2.622	1.769	2.346	2.622	2.154	2.344	1.965
$(K_2O)_{adj}$	5.932	6.799	6.050	8.173	5.841	5.728	6.392	5.921	5.789
$(P_2O_5)_{adj}$	0.018	0.030	0.020	0.031	0.034	0.022	0.032	0.029	0.012
Sum	100.00	100.00	100.00	100.00	100.00	100.00	100.00	100.00	100.00
Q	29.04	24.48	28.77	22.06	27.71	30.01	26.09	29.51	30.99
Or	35.05	40.18	35.75	48.30	34.52	33.85	37.77	34.99	34.21
Ab	26.05	21.69	22.19	14.97	19.85	22.19	18.22	19.83	16.63
An	4.49	5.64	5.06	3.87	3.23	3.18	1.56	3.55	1.38
C	1.75	5.01	4.59	9.41	11.30	8.80	14.67	9.40	14.53
Hy-Mg	0.10	0.10	0.10	0.10	0.10	0.10	0.10	0.10	0.10
Hy-Fe	2.17	1.69	2.08	0.61	1.88	1.08	0.89	1.48	1.28
Mt	1.09	0.86	1.10	0.36	1.00	0.58	0.47	0.81	0.68
Il	0.22	0.28	0.30	0.26	0.33	0.17	0.15	0.27	0.19
Ap	0.04	0.07	0.05	0.07	0.08	0.05	0.07	0.07	0.03
Mg#	4.36	5.56	4.64	12.27	4.85	7.83	9.56	5.74	6.79
FeO^t/Mg O	56.76	43.86	53.15	18.48	50.76	30.40	24.46	42.48	35.47
ASI	1.13	1.37	1.36	1.71	1.99	1.75	2.33	1.81	2.45
A/NK	1.65	1.99	2.00	2.27	2.77	2.45	3.01	2.54	3.16
Trace and rare earth elements									
Ba	131	352	183	354	249	99	135	298	84
Co	1	1	1	2	2			1	1
Cr	30			20					
Cs	31.1	43.6	28.2	19.1	31.6	28.8	29.2	37	34.5
Ga	37	35	36	27	39	39	43	38	41
Hf	10.6	9.3	11.4	3.4	12.2	11.6	10	10.4	8.3

Table 2 (continued)

Sample	GA-01	GA-02	GA-03	GA-04	GA-05	GA-06	GA-07	GA-08	GA-09
Rock (TAS)	Granite	Syeno-granite	Granite	Syeno-granite	Syeno-granite	Granite	Syeno-granite	Syeno-granite	Syeno-granite
Long. (°W)	22° 39′ 56"	22° 39′ 58"	22° 39′ 59"	22° 39′ 59"	22° 40′ 01"	22° 39′ 59"	22° 39′ 58"	22° 39′ 55"	22° 39′ 48"
Lat. (°N)	100° 25′ 01"	100° 24′ 58"	100° 24′ 58"	100° 24′ 58"	100° 24′ 54"	100° 25′ 01"	100° 25′ 01"	100° 25′ 14"	100° 25′ 18"
Nb	90	65	85	29	95	99	93	70	73
Pb	34	43	34	15	67	38	38	48	26
Rb	549	455	475	317	476	514	526	458	543
Sb	0.5	0.5		0.9	0.9				
Sr	16	39	22	39	35	16	17	40	13
Ta	12.3	9.7	10.8	3.9	12.9	14.5	13.4	10.3	13.5
Th	61.1	57	63.7	21.8	75.3	79.8	77.7	64.2	48.9
U	16.3	16.8	21.1	7.6	23.7	32.8	20.5	17.4	10.8
Y	152	111	158	63	143	130	71	87	41
Zn	70	170	100	70	180	70	60	180	100
Zr	263	278	345	108	401	290	247	338	213
La	69	89.5	97.8	39.4	143	65.7	56.7	96.1	50
Ce	145	217	193	79.7	324	146	154	212	183
Pr	19.4	22.6	25.4	9.62	39.8	18.5	15.2	24	12.8
Nd	75.3	84.8	99.8	37.7	145	72.8	56.4	88.1	44.9
Sm	20.3	18	24.4	9.1	31.4	18	12.1	18.8	9.4
Eu	0.49	0.83	0.78	0.76	1.52	0.42	0.42	0.88	0.4
Gd	18.4	14.5	22.2	8.6	21.4	16	9.5	14.1	6.6
Tb	3.6	2.6	4.1	1.6	4.3	3.1	1.9	2.6	1.2
Dy	22.9	16.3	25.2	10.3	27.1	19.9	12.6	15.6	6.9
Ho	4.6	3.2	4.8	2	4.9	4	2.6	3	1.4
Er	14.2	9.7	14.1	6.3	14.6	12.2	7.8	9.1	4.2
Tm	2.18	1.51	2.17	0.91	2.35	1.92	1.25	1.36	0.65
Yb	15	10.5	14.1	5.8	16.8	13.1	8.7	9	4.5
Lu	2.23	1.61	2.13	0.88	2.56	1.98	1.33	1.4	0.7
TREE	389.70	476.35	504.78	202.37	751.63	373.72	327.90	480.44	319.75
$(La/Yb)_{CN}$	3.13	5.80	4.72	4.62	5.79	3.41	4.44	7.27	7.56
$(La/Sm)_{CN}$	2.13	3.12	2.51	2.71	2.85	2.29	2.94	3.20	3.33
$(Gd/Yb)_{CN}$	0.99	1.12	1.28	1.20	1.03	0.99	0.89	1.27	1.19
$(Th/Yb)_{N}$	22.60	30.11	25.06	20.85	24.86	33.79	49.54	39.57	60.28
$(Y/Nb)_{N}$	0.27	0.27	0.30	0.35	0.24	0.21	0.12	0.20	0.09
$(La/Nb)_{N}$	0.81	1.46	1.22	1.44	1.59	0.70	0.64	1.45	0.72
$(Ce/Pb)_{N}$	0.38	0.45	0.51	0.48	0.43	0.34	0.36	0.40	0.63
(Ce/Ce*)	0.95	1.14	0.92	0.96	1.03	1.00	1.25	1.04	1.71
(Eu/Eu*)	0.08	0.15	0.10	0.26	0.17	0.07	0.12	0.16	0.15
(Nb/Nb*)	2.08	0.99	1.39	0.74	1.07	2.48	2.52	1.06	2.37
(Ta/Ta*)	5.26	2.74	3.27	1.84	2.70	6.73	6.71	2.88	8.12

Table 2 (continued)

Sample	GA-10	GA-11	GA-12	GA-13	GA-14	GA-15	GA-16	GA-17	GA-18	GA-19	GA-20
Rock (TAS)	Granodiorite	Granodiorite	Granite	Granite	Granite	Granite	Granite	Granite	Granite	Granite	Granite
Long. (°W)	22° 39′ 47"	22° 39′ 46"	22° 39′ 46"	22° 39′ 44"	22° 39′ 15"	22° 39′ 25"	22° 39′ 26"	22° 39′ 26"	22° 39′ 20"	22° 39′ 26"	22° 39′ 24"
Lat. (°N)	100° 25′ 18"	100° 25′ 18"	100° 25′ 18"	100° 25′ 15"	100° 25′ 29"	100° 25′ 27"	100° 25′ 31"	100° 25′31"	100° 25′26"	100° 25′ 32"	100° 25′31"
Major elements											
SiO_2	64.984	68.353	69.333	69.263	74.877	69.876	72.294	73.618	69.189	74.191	71.711
TiO_2	0.171	0.162	0.037	0.145	0.082	0.137	0.126	0.109	0.129	0.093	0.104
Al_2O_3	24.674	20.756	20.178	19.441	15.374	19.674	17.513	15.878	21.475	15.889	18.531
$Fe_2O_3^t$	1.614	1.876	0.781	1.703	0.37	1.562	1.713	1.891	0.791	1.73	1.434
MnO	0.035	0.053	0.048	0.083	0.029	0.058	0.069	0.088	0.037	0.103	0.066
MgO	0.039	0.039	0.037	0.038	0.036	0.038	0.037	0.038	0.037	0.037	0.037
CaO	0.488	0.549	0.773	0.743	1.776	0.406	0.398	0.609	0.282	0.325	0.37
Na_2O	1.991	2.047	2.384	1.859	2.656	2.144	2.304	2.21	1.992	2.181	2.139
K_2O	4.952	5.311	5.773	6.127	4.214	5.26	4.921	4.87	5.167	4.801	4.936
P_2O_5	0.018	0.026	0.01	0.034	0.008	0.016	0.008	0.011	0.011	0.008	0.007
LOI	0.44	0.28	0.377	0.068	0.093	0.276	0.117	0.169	0.311	0.134	0.149
Sum	99.41	99.45	99.73	99.50	99.52	99.45	99.50	99.49	99.42	99.49	99.48
Adjusted value											
$(SiO_2)_{adj}$	65.742	69.020	69.822	69.738	75.332	70.537	72.830	74.218	69.849	74.760	72.263
$(TiO_2)_{adj}$	0.173	0.164	0.037	0.146	0.082	0.138	0.127	0.110	0.130	0.094	0.105
$(Al_2O_3)_{adj}$	24.962	20.959	20.320	19.574	15.467	19.860	17.643	16.007	21.680	16.011	18.674
$(Fe_2O_3)_{adj}$	0.432	0.501	0.244	0.532	0.116	0.489	0.535	0.592	0.248	0.541	0.448
$(FeO)_{adj}$	1.080	1.253	0.488	1.064	0.231	0.979	1.071	1.183	0.496	1.082	0.897
$(MnO)_{adj}$	0.035	0.054	0.048	0.084	0.029	0.059	0.070	0.089	0.037	0.104	0.067
$(MgO)_{adj}$	0.039	0.039	0.037	0.038	0.036	0.038	0.037	0.038	0.037	0.037	0.037
$(CaO)_{adj}$	0.494	0.554	0.778	0.748	1.787	0.410	0.401	0.614	0.285	0.327	0.373
$(Na_2O)_{adj}$	2.014	2.067	2.401	1.872	2.672	2.164	2.321	2.228	2.011	2.198	2.155
$(K_2O)_{adj}$	5.010	5.363	5.814	6.169	4.240	5.310	4.957	4.910	5.216	4.838	4.974
$(P_2O_5)_{adj}$	0.018	0.026	0.010	0.034	0.008	0.016	0.008	0.011	0.011	0.008	0.007
Sum	100.00	100.00	100.00	100.00	100.00	100.00	100.00	100.00	100.00	100.00	100.00
Q	33.15	34.52	31.58	33.03	39.59	36.16	38.81	40.37	37.30	42.01	39.30
Or	29.61	31.69	34.36	36.46	25.05	31.38	29.30	29.01	30.83	28.59	29.39
Ab	17.04	17.49	20.31	15.84	22.61	18.31	19.64	18.85	17.02	18.60	18.24
An	2.33	2.58	3.80	3.49	8.81	1.93	1.94	2.97	1.34	1.57	1.80
C	15.37	10.81	8.69	8.54	3.25	9.85	7.75	5.94	12.23	6.58	9.08
Hy-Mg	0.10	0.10	0.09	0.10	0.09	0.10	0.09	0.10	0.09	0.09	0.09
Hy-Fe	1.41	1.72	0.72	1.43	0.25	1.27	1.44	1.67	0.56	1.58	1.23
Mt	0.63	0.73	0.35	0.77	0.17	0.71	0.78	0.86	0.36	0.78	0.65
Il	0.33	0.31	0.07	0.28	0.16	0.26	0.24	0.21	0.25	0.18	0.20
Ap	0.04	0.06	0.02	0.08	0.02	0.04	0.02	0.03	0.03	0.02	0.02
Mg#	6.11	5.30	11.98	6.02	21.84	6.53	5.84	5.46	11.84	5.79	6.90
FeO^t/MgO	37.24	43.28	18.99	40.33	9.25	36.99	41.66	44.78	19.24	42.07	34.87
ASI	2.60	2.06	1.75	1.77	1.27	1.98	1.78	1.59	2.30	1.70	1.95
A/NK	3.55	2.82	2.47	2.43	2.24	2.66	2.42	2.24	3.00	2.28	2.62
Trace and rare earth elements											
Ba	224	294	11	317	69	40	48	50	38	119	33
Co	1	1		1			1	1	1	1	1

Table 2 (continued)

Sample	GA-10	GA-11	GA-12	GA-13	GA-14	GA-15	GA-16	GA-17	GA-18	GA-19	GA-20
Rock (TAS)	Granodiorite	Granodiorite	Granite	Granite	Granite	Granite	Granite	Granite	Granite	Granite	Granite
Long. (°W)	22° 39′ 47"	22° 39′ 46"	22° 39′ 46"	22° 39′ 44"	22° 39′ 15"	22° 39′ 25"	22° 39′ 26"	22° 39′ 26"	22° 39′ 20"	22° 39′ 26"	22° 39′ 24"
Lat. (°N)	100° 25′ 18"	100° 25′ 18"	100° 25′ 18"	100° 25′ 15"	100° 25′ 29"	100° 25′ 27"	100° 25′ 31"	100° 25′31"	100° 25′26"	100° 25′ 32"	100° 25′31"
Cr		30		30				20	20	30	20
Cs	16	20.4	30.2	25.9	4.3	22.8	25.2	19.6	15.1	18.5	16.7
Ga	39	37	59	34	33	37	33	32	38	32	35
Hf	11.9	11.5	23.6	8.9	8.8	8.6	7.6	7.5	8.9	5.5	7.6
Nb	97	93	162	60	75	80	71	63	85	54	72
Pb	50	73	34	27	39	40	47	28	87	37	36
Rb	416	430	866	415	282	444	440	426	441	416	424
Sb	5.3	5.4	0.8		1.2	2.6	2	1.7	1.9		0.6
Sr	37	39	3	38	92	11	10	11	17	13	12
Ta	11.5	11.3	24.6	7.7	9.8	9.9	9.4	8.2	10.6	7.4	8.2
Th	67.9	67.1	93.5	53.7	50.4	45.6	58	40.4	50.7	28.3	48.9
U	12.8	18.1	13.1	15.2	18.9	7.4	17.4	7.1	14.8	11.3	23.2
Y	127	159	15	111	108	60	100	150	54	15	83
Zn	220	230	70	100	70	120	130	90	470	70	130
Zr	360	353	419	308	226	225	215	207	241	151	185
La	552.74	915.61	29.54	394.94	64.56	300.84	1042.19	628.69	416.46	124.05	683.54
Ce	515.50	639.48	61.66	314.85	57.26	159.71	182.71	274.06	226.75	104.08	179.45
Pr	355.60	610.99	17.35	254.31	55.82	226.29	647.63	478.45	270.47	80.60	433.19
Nd	271.33	470.46	13.35	188.84	55.80	178.99	448.58	371.99	204.38	56.89	317.29
Sm	27.5	51.6	1.7	19.3	9.6	20.7	43.5	44.3	20.7	5.4	30.6
Eu	185.81	348.65	11.49	130.41	64.86	139.86	293.92	299.32	139.86	36.49	206.76
Gd	16.16	50.27	1.78	15.10	3.37	6.39	16.52	11.37	6.75	3.55	9.59
Tb	108.54	182.41	8.04	77.89	57.79	72.86	135.18	162.31	69.35	18.59	103.02
Dy	108.03	177.29	11.08	77.56	66.48	66.48	119.11	149.58	60.94	16.62	91.41
Ho	95.93	141.06	10.57	68.70	65.85	51.63	83.74	118.29	47.97	13.41	70.33
Er	84.25	106.23	10.99	60.44	62.27	40.29	56.78	89.74	36.63	10.99	51.28
Tm	85.00	95.63	13.13	60.63	63.75	36.25	46.88	81.88	33.75	11.88	43.75
Yb	87.45	85.83	17.00	58.70	63.56	33.20	40.49	74.90	31.98	12.15	38.46
Lu	93.17	89.44	21.74	61.49	65.84	32.30	37.89	72.67	32.30	13.04	37.89
TREE	695.53	1017.62	63.59	460.80	132.07	324.77	718.35	647.30	407.47	141.82	529.88
$(La/Yb)_{CN}$	5.94	10.26	1.36	6.43	0.98	9.33	27.56	8.67	12.92	9.53	18.07
$(La/Sm)_{CN}$	2.98	2.63	2.58	3.04	1.00	2.16	3.56	2.11	2.99	3.41	3.32
$(Gd/Yb)_{CN}$	1.17	2.04	0.37	1.27	0.88	2.26	3.57	2.24	2.15	1.43	2.72
$(Th/Yb)_N$	25.11	25.85	148.19	30.09	26.38	48.64	52.74	19.15	54.08	74.75	44.47
$(Y/Nb)_N$	0.21	0.27	0.01	0.29	0.23	0.12	0.22	0.38	0.10	0.04	0.18
$(La/Nb)_N$	1.43	2.47	0.05	1.65	0.22	0.94	3.68	2.50	1.23	0.58	2.38
$(Ce/Pb)_N$	0.57	0.48	0.10	0.64	0.08	0.22	0.21	0.54	0.14	0.15	0.27
(Ce/Ce*)	1.14	0.84	2.63	0.97	0.95	0.61	0.22	0.50	0.66	1.02	0.32
(Eu/Eu*)	0.11	0.19	0.18	0.15	0.06	0.06	0.08	0.05	0.06	0.13	0.06
(Nb/Nb*)	1.20	0.72	37.93	0.91	6.43	2.01	0.53	0.77	1.57	2.49	0.82
(Ta/Ta*)	2.63	1.61	106.64	2.16	15.55	4.61	1.31	1.87	3.62	6.31	1.74

Table 2 (continued)

Sample	GA-21	GA-22	GA-23	GA-24	GA-25
Rock (TAS)	Granite	Granite	Granite	Granite	Granodiorite
Long. (°W)	22° 39′ 23"	22° 39′ 22"	22° 39′ 21"	22° 39′ 20"	22° 39′ 20"
Lat. (°N)	100° 25′ 31"	100° 25′ 28"	100° 24′ 27"	100° 25′ 25"	100° 25′ 26"
Major elements					
SiO_2	72.447	71.752	71.355	72.203	68.62
TiO_2	0.105	0.094	0.108	0.104	0.103
Al_2O_3	17.726	18.179	18.567	17.767	21.704
$Fe_2O_3^t$	1.484	1.639	1.364	1.374	1.171
MnO	0.058	0.082	0.059	0.069	0.051
MgO	0.037	0.037	0.038	0.037	0.038
CaO	0.492	0.575	0.673	0.59	0.299
Na_2O	2.153	2.056	2.263	2.122	2.054
K_2O	4.751	4.916	4.812	5.106	5.028
P_2O_5	0.009	0.008	0.007	0.007	0.009
LOI	0.206	0.14	0.217	0.113	0.324
Sum	99.47	99.48	99.46	99.49	99.40
Adjusted value					
$(SiO_2)_{adj}$	73.061	72.313	71.965	72.724	69.320
$(TiO_2)_{adj}$	0.106	0.095	0.109	0.105	0.104
$(Al_2O_3)_{adj}$	17.876	18.321	18.726	17.895	21.925
$(Fe_2O_3)_{adj}$	0.464	0.513	0.427	0.429	0.313
$(FeO)_{adj}$	0.929	1.025	0.854	0.859	0.783
$(MnO)_{adj}$	0.058	0.083	0.060	0.069	0.052
$(MgO)_{adj}$	0.037	0.037	0.038	0.037	0.038
$(CaO)_{adj}$	0.496	0.579	0.679	0.594	0.302
$(Na_2O)_{adj}$	2.171	2.072	2.282	2.137	2.075
$(K_2O)_{adj}$	4.791	4.954	4.853	5.143	5.079
$(P_2O_5)_{adj}$	0.009	0.008	0.007	0.007	0.009
Sum	100.00	100.00	100.00	100.00	100.00
Q	40.43	39.36	38.10	38.76	36.63
Or	28.31	29.28	28.68	30.39	30.02
Ab	18.37	17.53	19.31	18.09	17.56
An	2.40	2.82	3.32	2.90	1.44
C	8.24	8.52	8.50	7.75	12.49
Hy-Mg	0.09	0.09	0.10	0.09	0.10
Hy-Fe	1.26	1.46	1.15	1.18	1.10
Mt	0.67	0.74	0.62	0.62	0.45
Il	0.20	0.18	0.21	0.20	0.20
Ap	0.02	0.02	0.02	0.02	0.02
Mg#	6.68	6.09	7.41	7.18	8.04
FeO^t/MgO	36.09	39.86	32.30	33.41	27.73
ASI	1.85	1.87	1.83	1.76	2.32
A/NK	2.57	2.61	2.62	2.46	3.06
Trace and rare earth elements					
Ba	40	36	51	95	34
Co	1	1	1	1	1
Cr	20	20			
Cs	32.6	29.3	18.2	17.2	15.8
Ga	34	33	34	32	36

Table 2 (continued)

Sample	GA-21	GA-22	GA-23	GA-24	GA-25
Rock (TAS)	Granite	Granite	Granite	Granite	Granodiorite
Long. (°W)	22° 39′ 23"	22° 39′ 22"	22° 39′ 21"	22° 39′ 20"	22° 39′ 20"
Lat. (°N)	100° 25′ 31"	100° 25′ 28"	100° 24′ 27"	100° 25′ 25"	100° 25′ 26"
Hf	7.8	7.7	8.4	6.9	6.5
Nb	67	67	74	60	66
Pb	30	38	54	95	85
Rb	444	452	402	407	433
Sb	0.5	0.7	1.6	1.8	1.7
Sr	16	9	13	13	11
Ta	11	9.4	8.4	7.1	10
Th	47.1	43.2	46.3	45	52.2
U	17.1	11.9	14.6	12.7	17.4
Y	116	164	143	144	98
Zn	100	120	200	190	190
Zr	211	192	215	182	169
La	822.78	620.25	376.79	426.16	666.67
Ce	161.66	207.18	205.55	252.85	187.60
Pr	544.18	459.05	298.49	318.97	545.26
Nd	391.68	365.43	247.26	253.83	435.45
Sm	37.9	43.6	31.5	31.7	53.1
Eu	256.08	294.59	212.84	214.19	358.78
Gd	9.95	11.19	7.64	9.41	14.39
Tb	131.16	170.35	131.16	131.66	166.83
Dy	119.11	157.89	130.19	127.42	141.27
Ho	93.90	123.58	106.91	103.25	100.41
Er	71.43	97.07	86.08	82.42	69.60
Tm	61.88	87.50	81.25	78.13	56.88
Yb	53.85	76.92	73.68	72.06	49.39
Lu	52.17	75.16	73.91	72.05	45.34
TREE	617.24	602.54	451.91	496.63	637.26
$(La/Yb)_{CN}$	15.80	8.27	5.11	5.93	14.73
$(La/Sm)_{CN}$	3.22	2.11	1.78	2.00	1.86
$(Gd/Yb)_{CN}$	2.52	2.27	1.78	1.83	3.69
$(Th/Yb)_{N}$	31.10	19.80	21.58	21.52	39.67
$(Y/Nb)_{N}$	0.28	0.39	0.31	0.38	0.24
$(La/Nb)_{N}$	3.08	2.32	1.28	1.78	2.53
$(Ce/Pb)_{N}$	0.30	0.30	0.21	0.15	0.12
(Ce/Ce*)	0.24	0.38	0.61	0.68	0.31
(Eu/Eu*)	0.05	0.05	0.04	0.05	0.05
(Nb/Nb*)	0.64	0.84	1.48	1.03	0.77
(Ta/Ta*)	1.94	2.19	3.12	2.25	2.17

Major elements in weight percent and trace and rare earth elements in ppm

granodiorite samples display a peraluminous trend (Fig. 5b) with $(SiO_2)_{adj}$ values of 65.74–69.32 wt%, $(Al_2O_3)_{adj}$ of 20.96–24.96 wt%, $(CaO_2)_{adj}$ of 0.30–0.55 wt% and $(K_2O)_{adj}$ of 5.01–5.36 wt% (Table 2). The granodiorite rocks indicate A/NK and A/CNK ratio values of 2.82–3.55 and 2.62–3.32, respectively (Fig. 5b).

Trace element and rare earth-element (REE) concentrations are plotted in chondrite-normalized REE and primitive mantle-normalized multi-element diagrams (Fig. 6a–f). The granite rocks display Ba contents = 11–317 ppm, Rb = 282–866 ppm, Sr = 3–92 ppm and Zr = 151–419 ppm (Table 2). Chondrite normalized REE diagram (Fig. 6a) indicates enrichment in light REE (LREEs; $[La/Sm]_N = 0.99–3.55$) and heavy REEs (HREEs), as well, a strong negative Eu anomaly (Eu/Eu* = 0.04–0.18). On the primitive mantle-normalized multi-element diagram the granitic samples (Fig. 6b), display enriched patterns in incompatible elements with Nb (Nb/Nb* = 0.20–37.93), Ta (Ta/Ta* = 0.35–106), and P anomalies (Fig. 6b).

The syeno-granite samples show composition values of Ba = 84–354 ppm, Sr = 13–40 ppm, Rb = 317–543 ppm and Zr = 108–401 ppm. The chondrite-normalized REE patterns are (Fig. 6c) similar to granite samples, display enrichment in LREEs ($[La/Sm]_N = 2.70–3.32$) and HREEs with negative anomalies of Eu (Eu/Eu* = 0.11–0.26). Primitive mantle normalized diagram (Fig. 6d) shows an enriched pattern in incompatible elements with anomalies of Nb (Nb/Nb* = 0.03–2.51), Ta (Ta/Ta* = 0.04–8.11), and P anomalies (Fig. 6d).

The granodiorite samples display values of Ba = 34–294 ppm, Sr = 11–39 ppm, Rb = 416–433 ppm and Zr = 169–360 ppm (Table 2). Similarly to the granite and syeno-granite samples the chondrite-normalized REE diagram (Fig. 6e) from the granodiorite rocks displays an enriched LREEs ($[La/Sm]_N = 1.86–2.97$) and HREEs with negative anomalies of Eu (Eu/Eu* = 0.05–0.19). The primitive mantle normalized diagram shows enriched patterns in incompatible elements with anomalies of Nb (Nb/Nb* = 0.16–1.2), Ta (Ta/Ta* = 0.21–2.63), and P (Fig. 6f).

4.3 Zircon LA-ICP-MS U–Pb dating

Sample GA-03 was selected for zircon U–Pb geochronology. Zircon grains are elongated, optically clear ≤ 150 µm in maximum length. Oscillatory concentric zoning is noticeable on cathodoluminescence images (Fig. 7a). Nine zircons were analyzed by LA-ICP- SF-MS, and the results are plotted on the concordia diagram (Fig. 7a). Most analyses reveal Th/U ratios that are between 0.49 and 1.3. The U–Pb dating values are listed in Table 3. Nine spot analyses yielded a regression with the lower intercept at 31.70 ± 0.50 Ma (MSWD = 1.7), whereas three of the most concordant grains yielded the weighted mean $^{206}Pb/^{238}U$ ages of 31.4 ± 2.1 Ma (MWSD = 3.5, probability of fit = 0.031; Fig. 7c). We suggest 31.40 Ma as the average calculated age of the granite.

5 Discussion

5.1 Magmatic events

The previous K–Ar, Ar–Ar and U–Pb ages of the Guadalcazar granite have been compiled from the following references: Chryssoulis and Rankin, (1988; n = 1); Tuta et al., (1988; n = 4); and Díaz-Bravo et al. (2022; n = 1). Furthermore, the new U–Pb age data reported in this study compared to previous published age data show that magmatism through the Guadalcazar area has lasted from 34.7 to 28.3 Ma (Fig. 8). Regionally, four magmatic events have been recorded during the Paleogene between 60 and 23 Ma (Orozco-Esquivel et al., 2002; Nieto Samaniego et al., 2005). The first is associated with plutonic bodies of granodioritic and rhyolitic composition (La Tesorera, Peñon Blanco, San Pedro, Comanja) whereas the second is associated with andesitic and rhyolitic volcanism between 40 and 36 Ma that interbedded with continental sediments (Labarthe Hernández et al., 1982; Orozco-Esquivel et al., 2002; Nieto Samaniego et al., 2005); the third and most voluminous magmatism occurred between 34 and 27 Ma, with prominently rhyolitic composition magmatism with few and small interbedded mafic and intermediate composition effusions, which has been (Labarthe Hernández et al. al, 1982; Rodríguez-Ríos & Torres-Aguilera, 2009), finally, the fourth and last magmatic event occurred between 21 and 19 Ma with the generation of mafic and felsic magmatic products (Labarthe Hernández et al., 1982; Torres-Hernández et al., 2006). These magmatic events have been related to different extensional regimes, especially, the most voluminous magmatism occurred in the region between 34 and 27 Ma, which has been associated with the development of basins and mountain ranges in Central Mexico (Henry & Aranda 1992; Labarthe-Hernández et al., 1982; Orozco-Esquivel et al., 2002; Nieto Samaniego et al., 2005). The emplacement of the Guadalcazar intrusive occurred during 34–28 Ma, which suggests that this intrusive body can be related to the voluminous felsic magmatism occurred during the late Eocene and Oligocene in the southern region of the MC under different petrogenetic conditions related to the style of magmatic processes (Torres-Sánchez et al., 2020; Tristán-González et al., 2009). Nevertheless, the Guadalcazar intrusive marks an important area to keep studying in a petrology view, due to the different style of magmatic evolution compared to the volcanic products of surrounding areas.

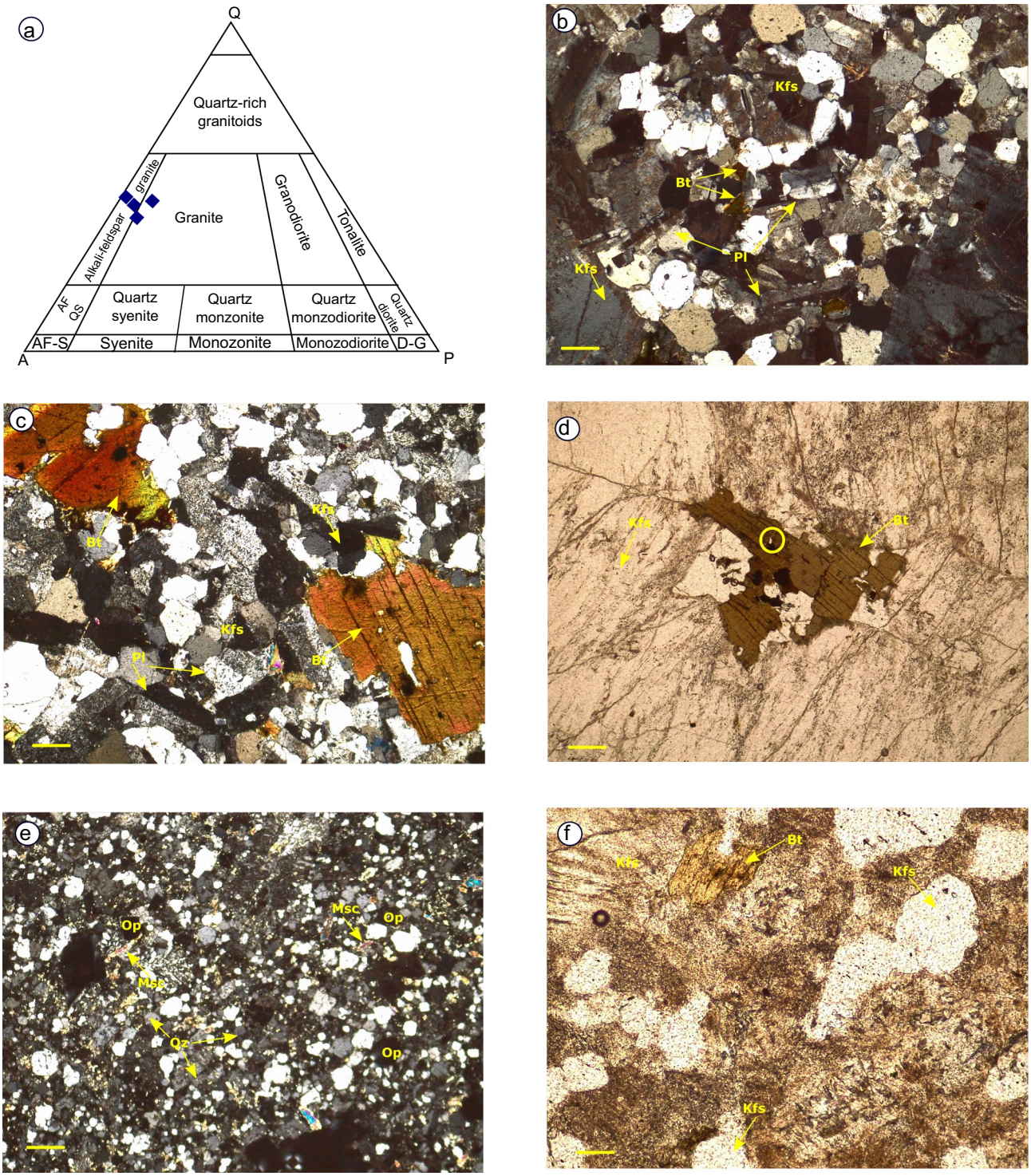

Fig. 4 Photomicrographs of the Guadalcazar granitic rocks. **a** QAP diagram shows an alkali-feldspar classification for the Guadalcazar intrusive rocks; **b** Phenocryst of potassic feldspar, biotite and plagioclase; **c** Phenocryst of biotite, potassic feldspar, and plagioclase with sieved textures; **d** Phenocryst of potassic feldspar, and biotite with pleochroic halo around zircon enclosed in biotite; **e** Coarse texture of granite sample showing muscovite microcrystals; **f** Phenocrysts of biotite and potassic feldspar in granite embedded in a phaneritic texture. Mineral nomenclature: Kfs potassic feldspar, *Pl* plagioclase, *Bt* biotite. QAP diagram nomenclature: *AF-S* alkali feldspar syenite, *AF-QS* quartz-alkali feldspar syenite, *D-G* Diorite-Gabbro

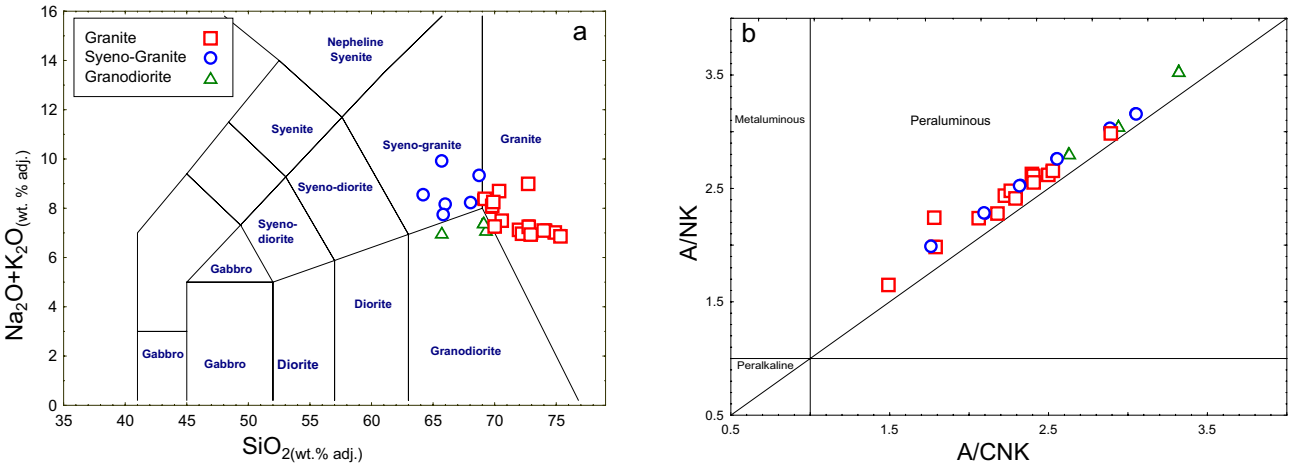

Fig. 5 a Total alkali-silica classification diagram (TAS; Le Bas et al., 1986); **b** A/CNK vs A/NK diagram for the plutonic rocks from the Guadalcazar area

5.2 Petrogenetic processes

5.2.1 Classification, origin and magma source

The studied granitic rocks display typical features of A-type magmas, showing high K_2O and high Ga/Al, FeO_T/($FeO_T + MgO$) and K_2O/($K_2O + Na_2O$) ratios. Accordingly, the combined ferroan character and the overall alkali-calcic to alkalic affinity for most of the samples from Guadalcazar (Fig. 9a, b; Frost et al., 2001) are consistent with the original, more restricted, definition of A-type granites firstly proposed by Loiselle and Wones (1979), later highlighted by Frost and Frost (2011). Furthermore, this is also supported by enrichment in alkalis, LREE, and HFSE and depletion in CaO and trace elements, which are compatible with mafic minerals (Co, Cr) and feldspars (Ba, Sr, Eu) in most samples. However, the elevated ASI of these rocks (range 1.13–2.6; Fig. 5b and Table 2) along with the presence of primary muscovite (up to 4.3 vol%; Table 1) are coherent with a strongly peraluminous character typical of S-type granites (e.g., Chappell & White, 2001). The plutonic rocks that share chemical features of A-type and S-type granites have been incrementally reported in the last decade (Dahlquist et al., 2013, 2014; Gao et al., 2020; Huang et al., 2011; Morales Cámera et al., 2017, 2018, 2020;), for which the term "peraluminous A-type granites" has been coined. The Guadalcazar granite besides sharing chemical compositions of A-type and S-type character indicated high Zr-saturation temperatures (869 ± 34 and 848 ± 45 °C; Boehnke et al., 2013; Watson & Harrison, 1983, respectively; Table 2) more typical of A-type granites (> 830 °C; King et al., 2001) rather than S-type (< 760 °C; Chappell & White, 2001; Chappell et al., 1998). In addition, the granitic samples also plot in the field of A-type granites in the discrimination diagrams of Whalen et al. (1987) (Fig. 10a–d). Consequently, we decided to classify them as peraluminous A-type granites, which is also supported by the Rb/Sr and Zr + Ce + Th values of the studied rocks, being more typical of peraluminous A-type granites than common orogenic S-type granites (Fig. 10e).

The origin and diversity of rocks that conform the A-type granites are still highly debated (e.g., Bonin, 2007; Dall'Agnol et al., 2012; Frost & Frost, 2011; Gao et al., 2020; Martin, 2006; Moreno et al., 2014), whose provenance varies between the mantle and crustal magmatic sources and metasedimentary sources (e.g., Bonin, 2007; Frost & Frost, 2011; Gao et al., 2020; Morales Cámera et al., 2020; Patiño Douce, 1997). The peraluminous nature of the Guadalcazar granite shows a crustal origin, which is corroborated by their A_2-type affinity (Eby, 1992; Fig. 11a–b), also supported by Y/Nb ratio values that are mostly higher than 1.4 (Table 2).

Other trace element ratios sensitive to magma sources have been also explored ($(Gd/Yb)_N$, (Eu/Eu)*, (Th/Yb), (La/Nb) and (Ce/Pb); McDonough & Sun, 1995; Moreno et al., 2014, 2016; Rudnick & Gao, 2003; Fig. 12a–c) to constrain the sources of the Guadalcaraz granite. The $(Gd/Yb)_N$ vs (Eu/Eu)* diagram suggests that the intrusive rocks from the Guadalcaraz probably derived from felsic sources of the upper continental crust (Fig. 12a). The studied samples mostly show $(La/Nb)_N$ vs $(Th/Yb)_N$ and $(Ce/Pb)_N$ vs $(Th/Yb)_N$ ratios similar to those of the continental crust (Fig. 12b, c). All these features are consistent with their strongly peraluminous character (ASI = 1.1–2.6; Fig. 5b and Table 2) and probable derivation from a continental crust source. Although it is important to highlight that the $(La/Nb)_N$ ratio is variable with several samples showing similar values to those of the OIB sources and that most of the samples also show $(Th/Nb)_N$ values higher than those of typical continental crust sources (Fig. 12b). The variation

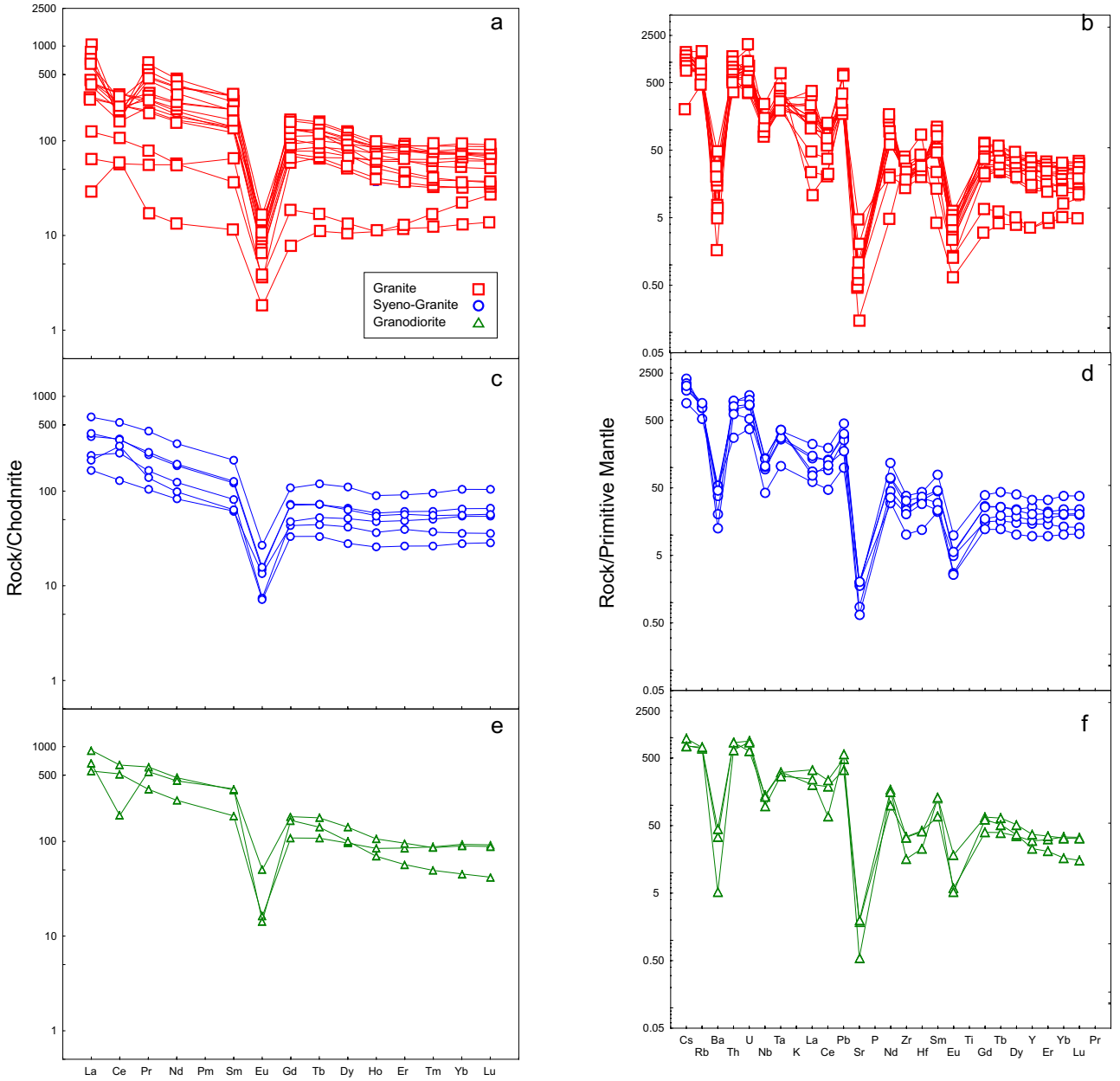

Fig. 6 **a**, **c**, **e** Chondrite-normalized rare-earth elements (REE) plot for the plutonic rocks from the Guadalcazar; **b**, **d**, **f** Primitive mantle-normalized multi-element diagram for plutonic rocks from the Guadalcazar. Values for normalization were taken from McDonough and Sun (1995). (See Fig. 5 for explanation of symbol legend)

in the La/Nb ratio may be explained by crystal fractionation of LREE-accessory minerals (Moreno et al., 2014, 2016; Troll et al., 2003) that depleted the melt in La with respect to Nb. This agrees well with the trends shown in Fig. 13b. The high Th/Nb ratios must be related to Th-LREE rich sources as discussed by Moreno et al. (2017) since segregated liquids from metalunimous and peraluminous sources tend to have the same or lower Th abundance than the source (Bea, 2012). Therefore, taking into account the strongly peraluminous nature of the Guadalcazar granite and that monazite is the major Th and LREE carrier in granites and metapelites (Bea, 1996), the high Th contents of these granites might be explained by the preferred dissolution of monazite during partial melting of monazite-bearing metasedimentary sources (Stepanov et al., 2012). Similar peraluminous A-type granite compositions, but with a less marked ferroan character, have originated through partial melting of metasedimentary rocks at low pressure ($P = < 0.8$GPa) and high temperature ($T = > 850$ ºC) under oxidizing conditions ($\geq$FMQ + 1) (Gao et al., 2020). Accordingly, the Guadalcazar granite

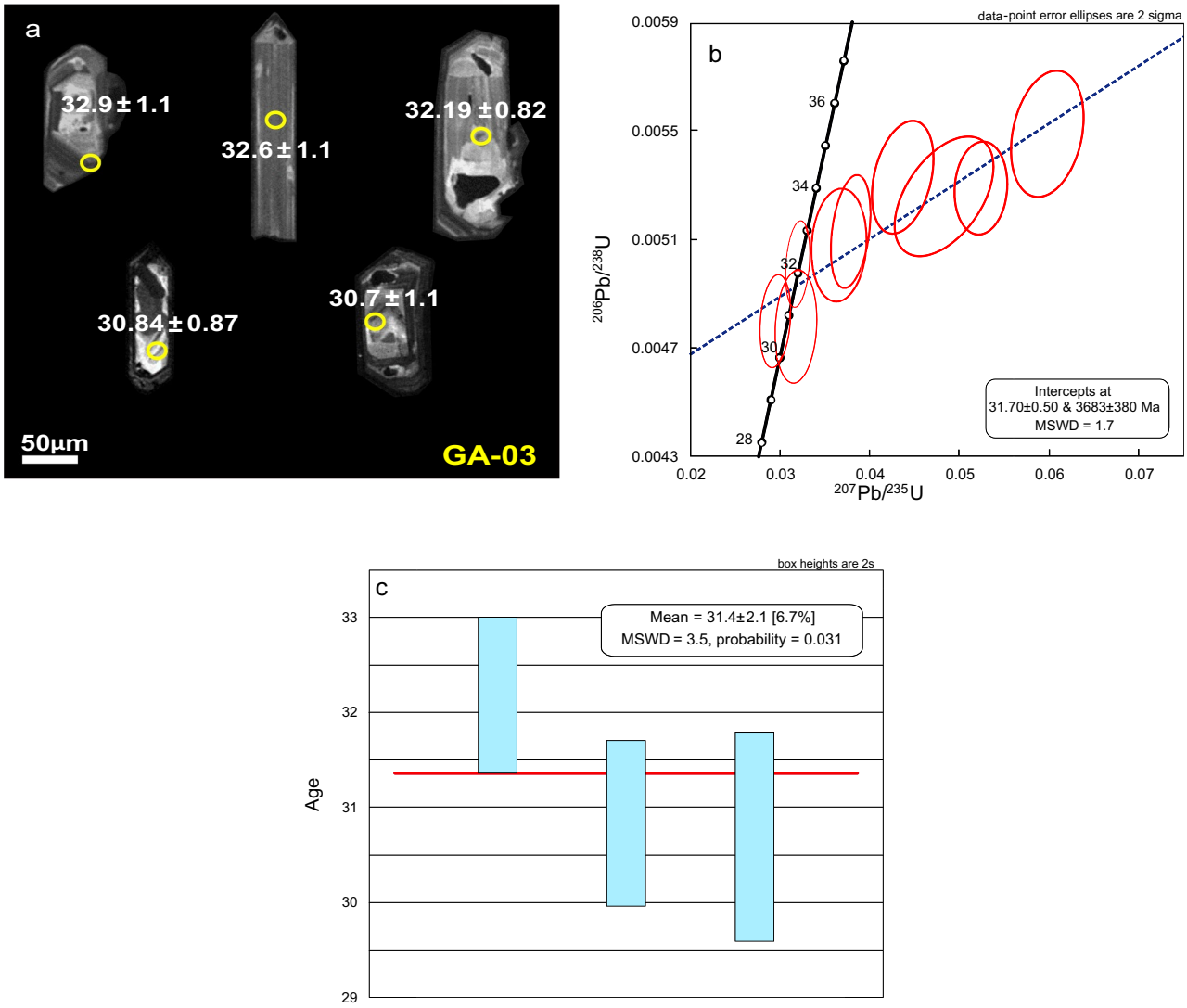

Fig. 7 **a** Cathodoluminescence (CL) and BSE images of zircons; **b** U–Pb concordia plot; **c** Mean age (weighted average, $^{206}Pb/^{238}U$ age) considered as crystallization age for the Guadalcazar granite

could have formed from a metasedimentary source at similar conditions but in a reduced environment (Fig. 13).

5.2.2 Fractional crystallization

In the absence of isotopic data, the role of fractional crystallization or partial melting can be best visualized by plotting the geochemical variables such as the ratios of relatively immobile elements ((La/Yb) vs La; La vs (La/Sm), and (Zr/Nb) vs Zr (Fig. 14a–c). These ratios were used to discriminate the magmatic processes that controlled the evolution of the Guadalcazar granite. All samples display a compositional trend mostly consistent with fractional crystallization rather than partial melting (Fig. 14a–c). The major and trace element variations with increasing SiO_2 content also indicate fractional crystallization processes (see in Supplementary material Figure S1a–g). Fractional crystallization of Fe–Ti oxides is reflected in SiO_2 vs TiO_2 and $Fe_2O_3{}^T$ (Figure S1a–b). Furthermore, most major and trace element contents are linearly correlated with SiO_2 content, whereas Na_2O and K_2O contents are negatively correlated (Figure S1c–d), which indicates fractional crystallization of alkali feldspar. A strong negative Eu anomaly is evident in the chondrite-normalized REE diagrams (Fig. 6a, c, e), suggesting large amounts of plagioclase in the source region. According to Clemens et al (1986), alkali feldspar has a lower crystallization temperature than plagioclase that may have formed throughout the entire interval of magmatic evolution. Such variation could be seen in Sr and Ba contents with increasing SiO_2 content, which suggests fractional crystallization of

Table 3 Results of U–Pb dating of zircons on granitic rocks from the Guadalcazar

Sample-spot		Content (mg.g-1)								Isotopic ratios							Isotopic ages (Ma)						% conc
	f206 (%)	U	2 s	Th	2 s	Pb	2 s	Th/U	206Pb/204Pb	207Pb/206Pb	2 s	207Pb/235U	2 s	206Pb/238U	2 s	Rho	207Pb/206Pb	2 s	206Pb/238U	2 s	207Pb/235U	2 s	
GA-03-3C	0.69	695	41	218	12	7.55	0.73	0.31	2705	0.1390	0.0680	0.0686	0.0052	0.0060	0.0002	0.34	1436	88	38.8	1.4	64.1	4.4	61
GA-03-16C	0.81	745	24	268.8	8.9	5.24	0.46	0.36	2305	0.0758	0.0091	0.0437	0.0028	0.0053	0.0002	0.33	963	70	34.2	1.1	42.6	2.6	80
GA-03-26C	0.61	1047	44	253	9	7.37	0.74	0.24	3055	0.0950	0.0110	0.0483	0.0045	0.0053	0.0002	0.49	1150	100	33.8	1.1	45.8	3.8	74
GA-03-25C	0.45	1497	58	500	19	10.4	0.78	0.33	4185	0.0551	0.0028	0.0379	0.0018	0.0051	0.0002	0.32	816	51	32.9	1.1	37.6	1.8	88
GA-03-23C	1.07	675	28	418	19	5.96	0.49	0.62	1750	0.2200	0.1200	0.0366	0.0025	0.0051	0.0002	0.10	1083	73	32.6	1.1	36.1	2.4	90
GA-03-29C	0.78	855	39	289	10	8.21	0.59	0.34	2405	0.0854	0.0052	0.0598	0.0033	0.0055	0.0002	0.26	1450	73	35.3	1.2	58.3	3.1	61
GA-03-40C	0.19	4240	210	1198	55	19.3	1.2	0.28	9870	0.0480	0.0018	0.0320	0.0011	0.0050	0.0001	0.25	498	34	32.19	0.82	31.9	1.1	101
GA-03-16r	0.19	4240	210	1198	55	19.3	1.2	0.28	9870	0.0480	0.0018	0.0320	0.0011	0.0050	0.0001	0.25	498	34	32.19	0.82	31.9	1.1	101
GA-03-7a	0.64	1407	84	416	21	6.61	0.57	0.30	2930	0.1030	0.0570	0.0318	0.0019	0.0048	0.0002	0.12	945	72	30.7	1.1	31.6	1.9	97

% conc = (206Pb-238U age/207Pb-206Pb age) *100; f206c (degree of concordance) = ($^{206}Pb^{204}Pb$model/$^{206}Pb^{204}Pb$ measured) × 100, Spot size = 25 µm, depth of crater ~ 20 µm

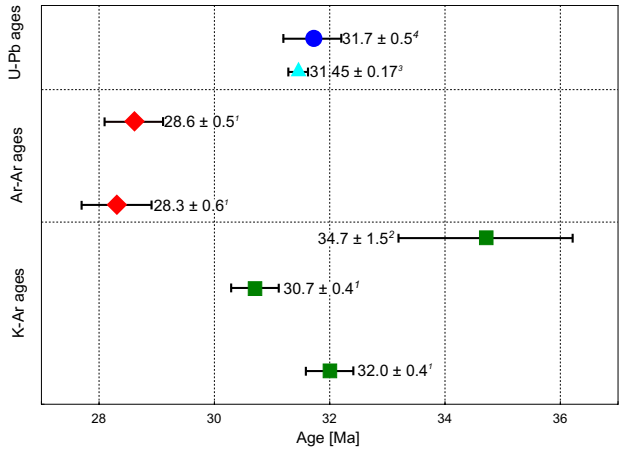

Fig. 8 Age distribution of the Guadalcazar plutonic body. Previous ages were taken from [1]Tuta et al. (1988), [2]Chryssoulis and Rankin, (1988), [3]Díaz-Bravo et al. (2022), [4]This work

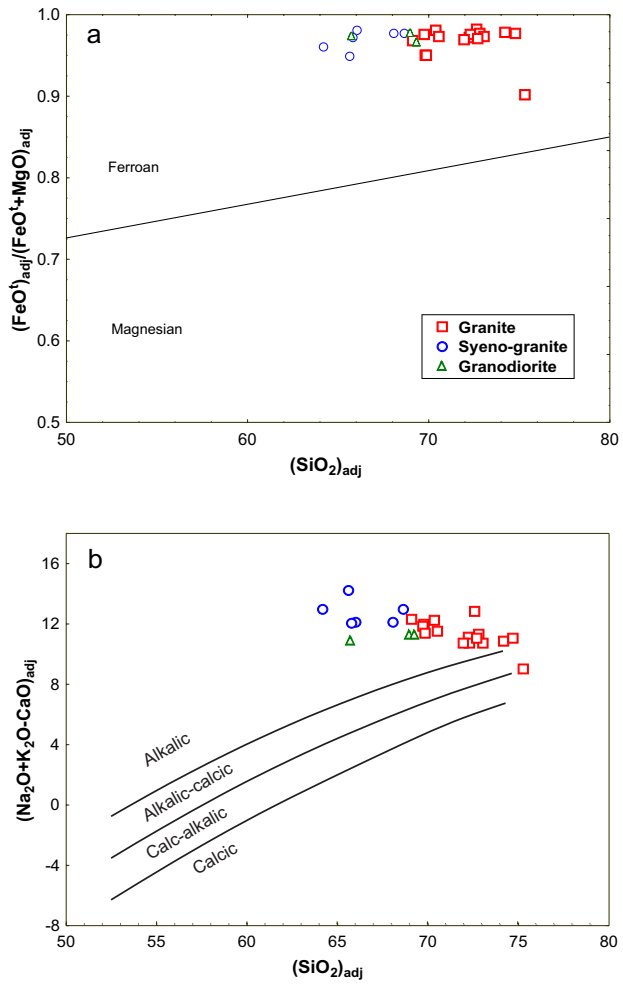

Fig. 9 **a** $(SiO2)_{adj}$ vs $[(FeO^t)_{adj}/(FeO^t+MgO)_{adj}]$ diagram. Gray area represnts A-type granite field, after Frost et al. (2001); **b** $(SiO2)_{adj}$ vs MALI-index diagram after Frost et al. (2001) for the Guadalcazar granite

alkali feldspar (Figure S1e–f). Zr with SiO_2 content, which reflects fractional crystallization of Fe–Ti oxides, zircon, and apatite (Figure S1g) Therefore, these factors, can suggest that the fractional crystallization was the main mechanism in the origin of the granite samples. Nevertheless, several immobile trace elements based on bivariate diagrams presented in Fig. 12a–c can suggest an evolved crustal source in the granitic genesis.

5.3 Tectonic setting

5.3.1 Nb and Ta anomalies

In the primitive-mantle normalized diagram (Fig. 6b, d, f), the behavior of Nb (a HFSE) with respect to its neighbor elements Ba (a LILE) and La (a light rare-earth element−LREE) can be quantified from the following equation (Verma, 2015):

$$\left[Nb/Nb^*\right]_{PM} = \frac{2\left(Nb_{sample}/Nb_{PM}\right)}{\left(Ba_{sample}/\left(Ba_{PM}\right) + \left(La_{sample}/\left(La_{PM}\right)\right)} \quad (1)$$

$$\left[Ta/Ta^*\right]_{PM} = \frac{2\left(Ta_{sample}/Ta_{PM}\right)}{\left(Ba_{sample}/\left(Ba_{PM}\right) + \left(La_{sample}/\left(La_{PM}\right)\right)} \quad (2)$$

where the element symbols Nb, Ta, Ba, and La refer to the concentrationof these elements in a sample or normalizing material; $[Nb/Nb^*]_{PM}$ and $[Ta/Ta^*]_{PM}$ refer to Nb- and Ta anomalies. The parameter $(Nb/Nb^*)_{pm}$ is generally called as Nb-anomaly. Any other normalization or calculation formula (such as geometric mean, instead of the simple mean) will only change the actual values, but not the conclusions. Ta-anomaly $[Ta/Ta^*]_{PM}$ can be similarly defined (Verma, 2015). In addition, the Nb- and Ta-anomalies are more meaningful for discriminating different tectonic settings because such elements are likely to have lesser crustal assimilation effects that affect the size of these anomalies. In the present study, we have calculated Nb and Ta anomalies size values for granitic rocks from the Guadalcazar area following the equations reported by Verma (2015), and the results are reported in Supplementary Table S1. Furthermore, compared our results to Nb and Ta anomalies value for basic, intermediate and acid rocks that were compiled from several tectonic settings worldwide (Verma, 2015). The calculated Nb and Ta anomalies values for granitic rocks from the Guadalcazar area were compared with the Nb and Ta anomalies values of Sierra de San Miguelito Volcanic Complex, Mexico (SSMC), Pinos Volcanic Complex, Mexico (PVC), Mesa Virgen Calerilla, Mexico (MVC), as well as, anomalies values proposed by Verma (2015) that are reported in Table S1. Results display that statistically calculated Nb and Ta anomalies size for the Guadalcazar

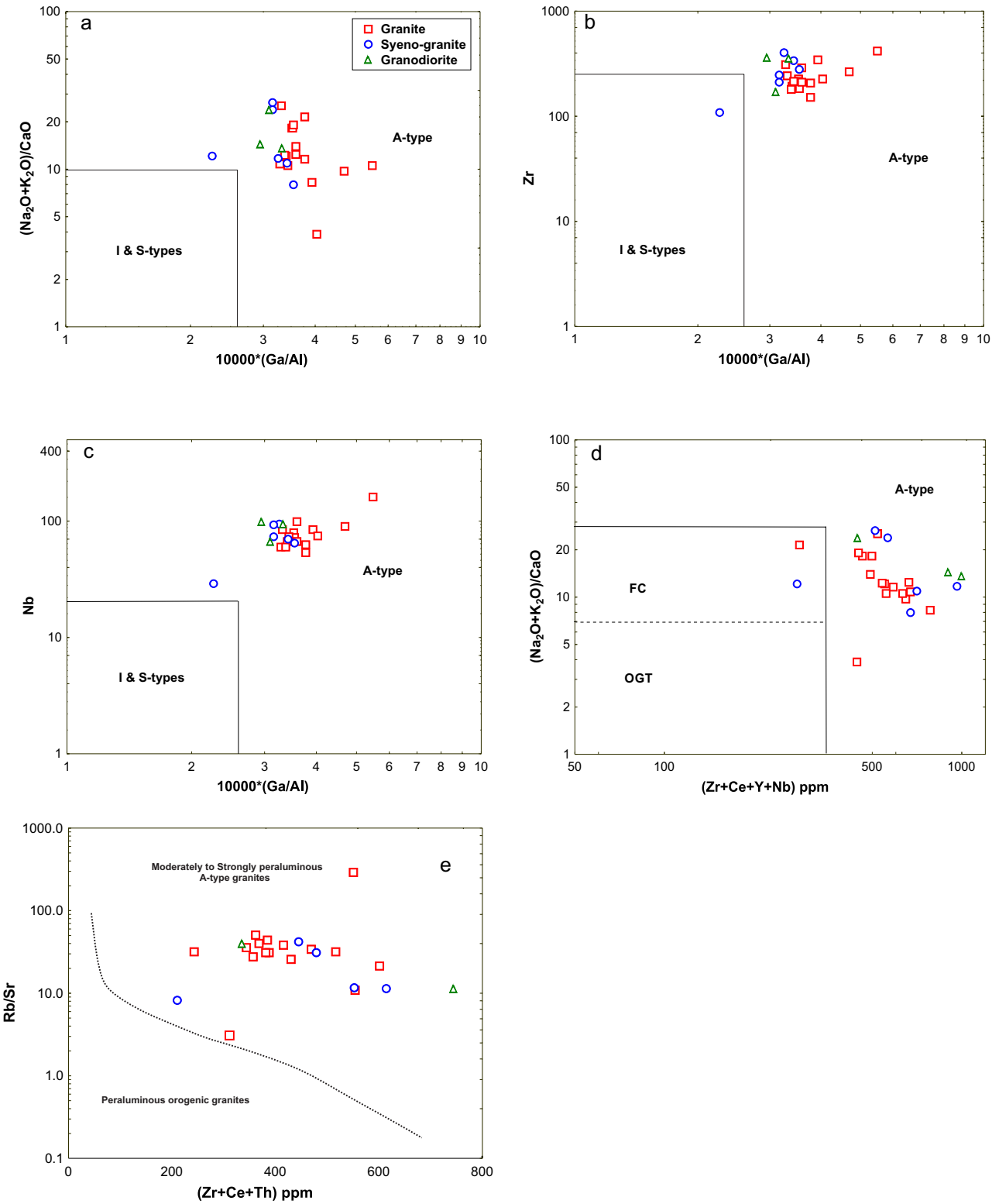

Fig. 10 **a**–**d** Granite discrimination diagrams from Whalen et al. (1987) for the Guadalcazar granite, **e** Zr + Ce + Th vs Rb/Sr granite discrimination diagram showing the compositions of the Guadalcazar granite. The dashed line divides moderately to strongly peraluminous A-type granites and peraluminous orogenic granites fields, respectively. *FC* fractionated felsic granites, *OTG* unfractionated I- and S type granites (OTG) from Whalen et al. (1987)

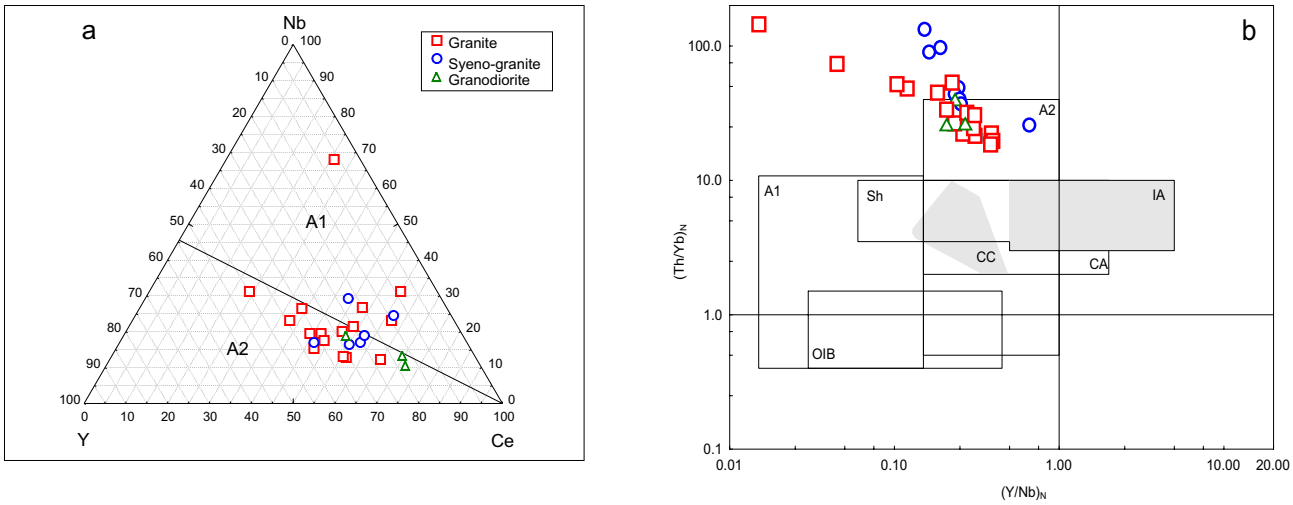

Fig. 11 **a** A-type granites discrimination diagrams from Eby (1992); **b** $(Y/Nb)_N$ vs $(Th/Yb)_N$ diagram for granites discrimination from Moreno et al. (2014) for the Guadalcazar granite. Normalization values after McDonough and Sun, (1995). *A1* A_1 type granite, *A2* A_2 type granite, *CA* Continental Arc, *CC* Continental Crust, *IA* Island Arc, OIB Ocean Island Basalt, *Sh* shoshonites

area (0.26 ± 0.01; 0.97 ± 0.17), which are higher or more-less similar to San Juan volcanic field (0.22 ± 0.05), USA, Lhasa terrane (0.232 ± 0.024; 0.284 ± 0.036), Tibet, Eastern Anatolia (0.50 ± 0.13; 0.680 ± 0.017), Turkey (Table S1). This finding suggests patterns of both anomalies (Nb and Ta) that are similar to most rifts and extension-related areas (Table S1).

5.3.2 Multidimensional tectonic discrimination diagrams

New multi−dimensional discrimination diagrams were used to infer the tectonic setting, because conventional bivariate and ternary diagrams for tectonic discrimination were shown to work unsatisfactorily (Verma, 2010). The failure of the older diagrams is based on the following criteria: (i) use of limited database to construct them; (ii) the problem of closed or constant sum compositional variables not attended in older diagrams; (iii) eye−fitted tectonic field boundaries in the older diagrams. All these problems have been discussed in the multidimensional solutions (Verma, 2015, 2017; Verma et al., 2012, 2013). Therefore, in this work, new immobile major-trace elements based multidimensional discrimination diagrams (Verma et al., 2013) for felsic rocks have been used to infer the plate tectonic setting of the Guadalcazar granite. These diagrams are based on natural logarithm transformed ratios and linear discrimination analysis (LDA) of chemical data, which make it more robust compared to conventional bivariate and ternary diagrams (Verma, 2020; Verma et al., 2012, 2020, 2021). The multidimensional discrimination diagrams for the Guadalcazar granite samples display a within-plate tectonic setting (Fig. 15a, b), because samples were plotted in the continental rift + ocean island (CR + OI) field. This finding could be also consistent with the geological evidence from the area that is related to the early stages of an extensional regime of the MC province. In addition, it could be recommended that for more constraints from this and surrounding plutonic areas the study of mafic rocks such as volcanic and mafic plutonic rocks and underlying crust and mantle is required before a comprehensive petrogenetic and tectonic model could be put forth. This is mainly considered for future studies.

5.3.3 Geodynamic model

Petrological, geochemical and geochronological observations reveal that the Guadalcazar granite was emplaced during the Oligocene (34–28 Ma), at a similar time of the emplacement of different felsic volcanic lithology around the San Luis Potosí Volcanic field (~ 33 to 27 Ma; Aguillón-Robles et al., 2014; Torres-Sánchez et al., 2020; Tristán-Gonzalez et al., 2009). It has been well documented that an extensional regime prevailed in the southern region of the MC during the Cenozoic (Aranda-Gómez et al., 2000; Labarthe-Hernández & Jiménez-López, 1992; Nieto-Samaniego et al., 1997). At the southern region of the MC, a variety of felsic volcanic rocks erupted, and this could support that partial melting of continental crust has occurred with the combination of different magmatic processes such as fractional crystallization and assimilation. Therefore, from the results and petrogenetic evidence derived from the present work can be inferred that the Guadalcazar granite was formed by the fractional crystallization of a magma source that was enriched by continental crust contributions. Another factor to consider in the magmatism of the southern

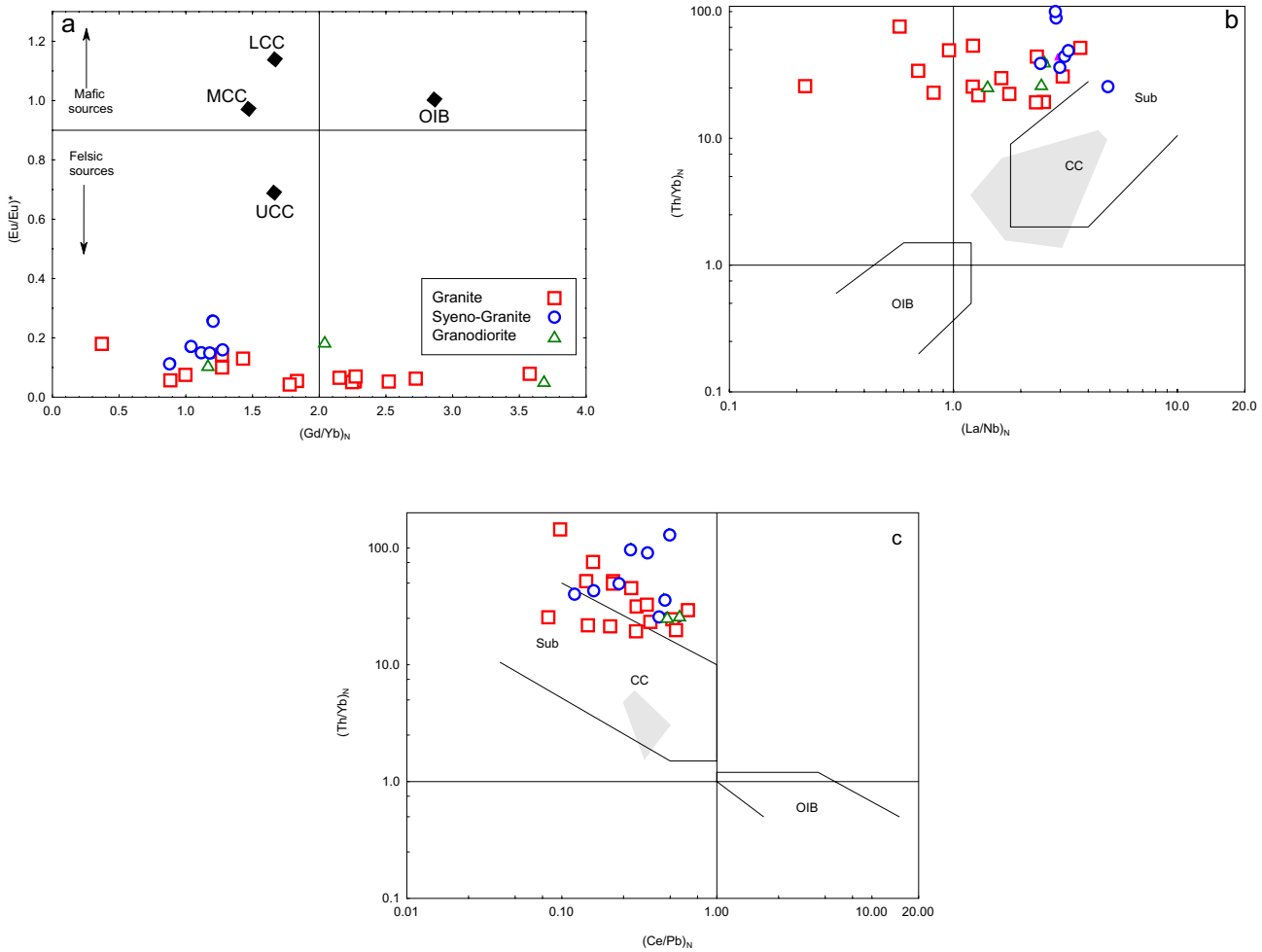

Fig. 12 **a** (Eu/Eu)* vs $(Gd/Yb)_N$ diagram; **b** $(La/Nb)_N$ vs $(Th/Yb)_N$ diagram; **c** $(Ce/Pb)_N$ vs $(Th/Yb)_N$ diagram from Moreno et al. (2014) for the magma sources to the Guadalcazar granite. Normalization values were taken from McDonough and Sun (1995). Values of LCC, MCC and UCC were taken from Rudnick and Gao (2003). *CA* Continental Arc, *CC* Continental Crust, *IA* Island Arc, *LCC* Lower Continental Crust, *MCC* Middle Continental Crust, *OIB* Ocean Island Basalt, *Sh* shoshonites, *Sub* subduction-related magmatic suites, *UCC* Upper Continental Crust

part of the MC is the high content of fluorine, uranium and/or tin, something that is shown as evidence of significant crustal contribution to felsic magmatism (Tuta et al., 1988; Burt et al., 1980; Finch, 1987). Figure 16 presents a schematic illustration of the thermo-magmatic evolution model of the Guadalcazar granite during the Oligocene in an extensional regime. This magmatism was mainly influenced by an extension process that induced thinning of the crust to the west of the Valles-San Luis Potosi platform and isostatic imbalance in the western part of it (Fig. 16). In addition, upwelling of the asthenosphere in response to extension favored the development of basaltic magmatism strongly interacted with continental crust, leading to its partial fusion and ultimate emplacement of granites with fluorine and/or tin mineralization (Fig. 16). Furthermore, Nieto-Samaniego et al. (1999) have proposed that the mechanism, which produced the extension and volcanism, was related to a retreating slab that generate a flux of the asthenosphere into the mantle wedge, which produce widespread melting at the base of the crust as well as intra-arc extension in the overriding plate, in this case, in the San Luis Potosí Volcanic Field area. As well as, these authors mentioned that boundary conditions determine the timing, magnitude and orientation of the extension regime, whereas the magmatism style is mainly controlled by the internal structure of crustal blocks and the thermal effects of magmatism (Nieto-Samaniego et al., 1999). Therefore, geochemical interpretation and petrogenetic evidence derived from this work, it can be inferred that the Guadalcazar granite was formed by the fractional crystallization of a magma source that was enriched with contributions of continental crust, and was emplaced in the core of Laramide anticline structure affected by different tectonic structure styles (i.e., fold structures and fault systems; Tuta et al., 1988; Burt et al., 1980; Finch, 1987).

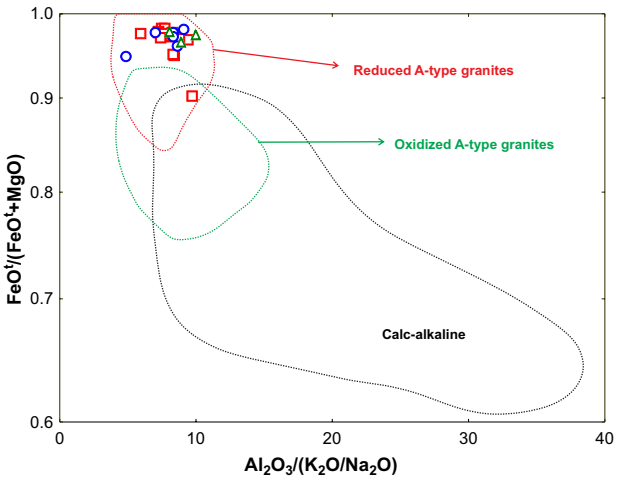

Fig. 13 Whole-rock diagram $(Al_2O_3)_{adj}/[(K_2O/Na_2O)_{adj}]$ vs $[(FeO^t)_{adj}/(FeO^t+MgO)_{adj}]$ shows the composition of representative oxidized and reduced A-type granites for the Guadalcazar granite. (See Fig. 5 for explanation of symbol legend)

6 Conclusion

Based on an integrated study of zircon geochronology (U–Pb) and whole rock geochemistry for the Guadalcazar granite, following conclusion can be summarized:

1. The Guadalcazar granite was emplaced in Oligocene time; U–Pb zircon dating yielded an average calculated age of 31.40 Ma.
2. Based on the geochemical data, we classified the Guadalcazar granite as strongly peraluminous A-type granites.
3. The Guadalcazar granite is characterized by enriched REE and HFSE; depleted Ba, Sr, P, Ti, and Eu anomalies. These A-type granites belong to typical A_2 type granites of crustal origin.
4. Geochemical data combined with literature data showed fractional crystallization rather than partial melting as the dominant petrogenetic process.

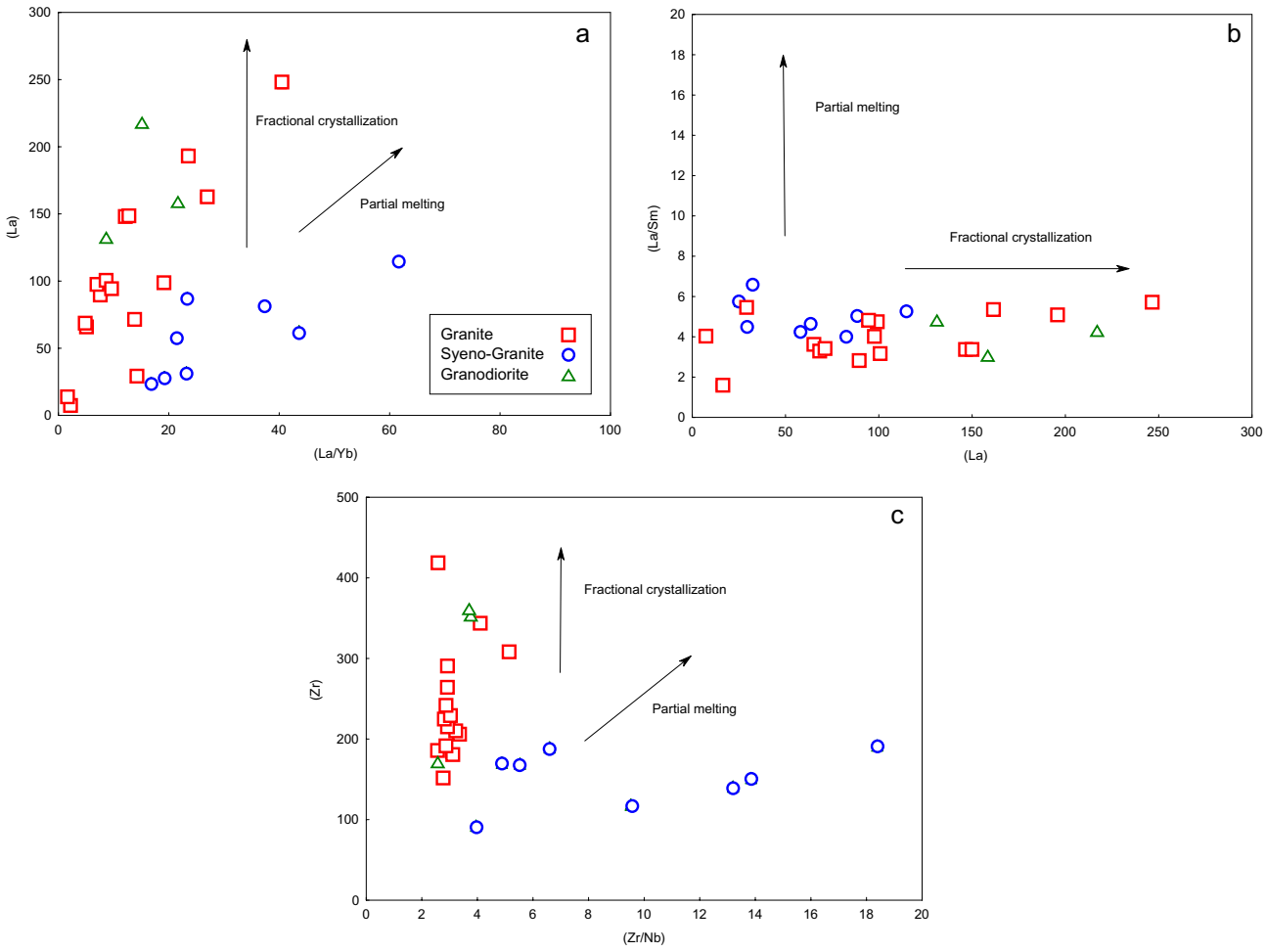

Fig. 14 **a** La vs (La/Yb); **b** La vs (La/Sm); **c** (Zr/Nb) versus Zr diagram illustrating the partial melting and fractionation effects for the origin of Guadalcazar granite

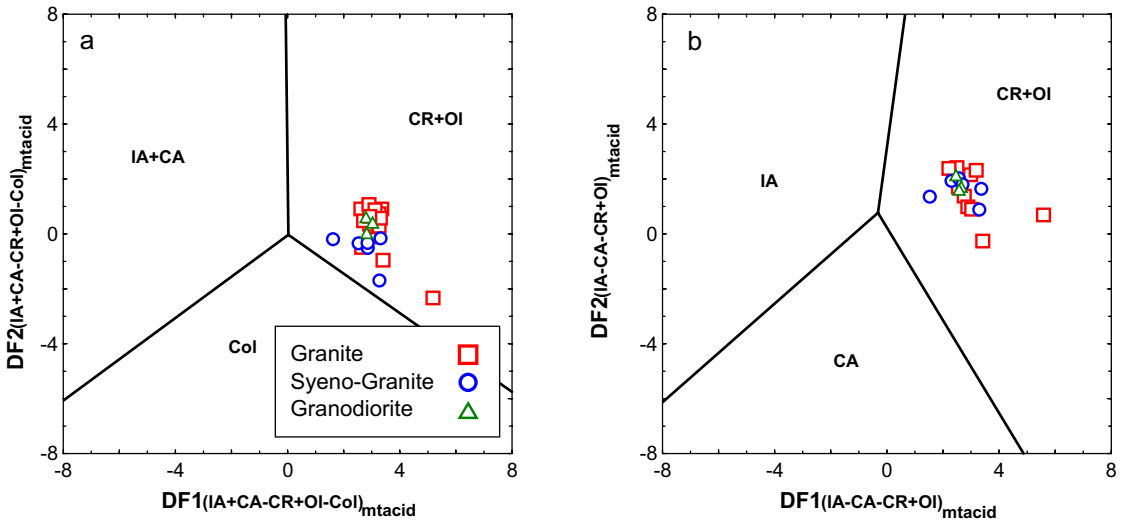

Fig. 15 **a**, **b** Discriminant−function multidimensional diagrams based on log−transformed ratios of major and trace elements for tectonic discrimination of granitic rocks from the Guadalcazar area (Verma et al., 2013). *IA + CA* Island Arc + Continental Arc (arc), *CR + OI* Continental Rift + Ocean Island (within-plate), *COL* Collision

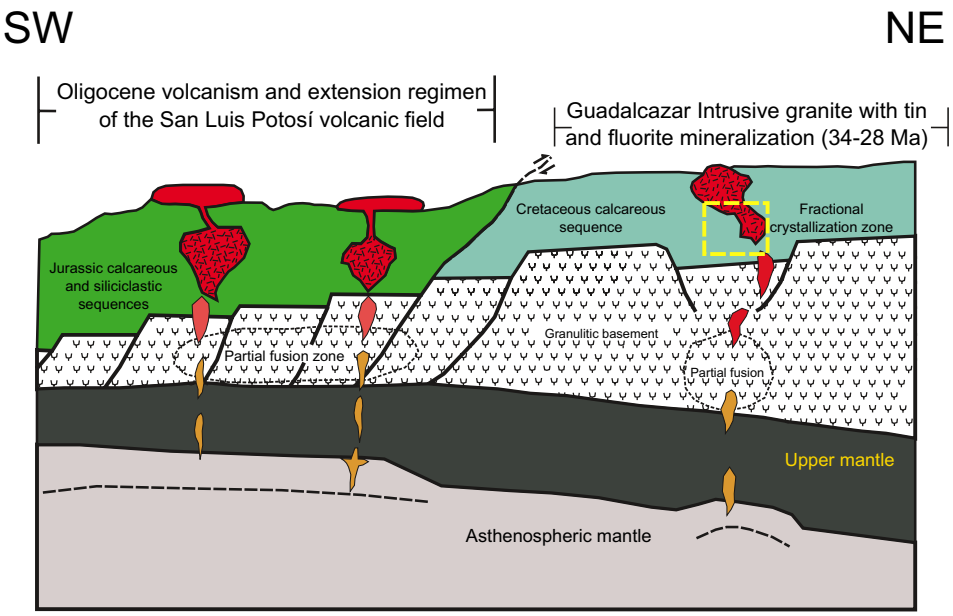

Fig. 16 Schematic thermo-magmatic model showing the generation and ascent of the magmas at the Guadalcazar area during the Oligocene

5. The Guadalcazar granite originated in an extensional tectonic setting consistent with the geological and geochemical evidences.

Supplementary Information The online version contains supplementary material available at https://doi.org/10.1007/s41513-022-00201-7.

Acknowledgements The first author (SKV) is grateful to Newton Advance Fellowship award–The Royal Society, UK for the grant [NA160116]. DALH is thankful to the National Council of Science and Technology (CONACYT), Mexico for his Master degree fellowship [grant 1007284]. We are grateful to two anonymous reviewer for helpful comments on an earlier version of this paper.

Declarations

Conflict of interest On behalf of all authors, the corresponding author states that there is no conflict of interest.

References

Aguillón-Robles, A., Tristán-González, M., Aguirre-Díaz, G. J., López-Doncel, R. A., Bellon, H., & Martínez-Esparza, G. (2014). Eocene to Quaternary mafic-intermediate volcanism in San Luis Potosí, central Mexico: The transition from Farallon plate subduction to intra-plate continental magmatism. *Journal of Volcanology and Geothermal Research, 276*, 152–172.

Angeles-Moreno, E., Nieto-Samaniego, A. F., Ruiz-González, F. J., Levresse, G., Alaniz-Alvarez, S. A., Olmos-Moya, M. D. J. P., & Miranda-Avilés, R. (2017). The transition between shortening and extensional regimes in central Mexico recorded in the tourmaline veins of the Comanja Granite. *Journal of South American Earth Sciences, 73*, 65–77.

Aranda-Gómez, J. J., Henry, C. D., & Luhr, J. F. (2000). Evolución tectonomagmática post-paleocénica de la Sierra Madre Occidental y de la porción meridional de la provincia tectónica de Cuencas y Sierras: México. *Boletín De La Sociedad Geológica Mexicana, 53*, 59–71.

Aranda-Gómez, J. J., Luhr, J. F., Housh, T. B., Valdez-Moreno, G., & Chávez-Cabello, G. (2007). Late Cenozoic intraplate-type volcanism in central and northern México: A review. *Special Papers-Geological Society of America, 422*, 93.

Barbarin, B. (1999). A review of the relationships between granitoid types, their origins and their geodynamic environments. *Lithos, 46*, 605–626.

Bea, F. (1996). Residence of REE, Y, Th and U in granites and crustal protoliths: Implications for the chemistry of crustal melts. *Journal of Petrology, 37*, 521–552.

Bea, F. (2012). The sources of energy for crustal melting and the geochemistry of heat producing elements. *Lithos, 153*, 278–291.

Boehnke, P., Watson, E. B., Trail, D., Harrison, T. M., & Schmitt, A. K. (2013). Zircon saturation re-revisited. *Chemical Geology, 351*, 324–334.

Bonin, B. (2007). A-type granites and related rocks: Evolution of a concept, problems and prospects. *Lithos, 97*, 1–29.

Burt, D. M., Sheridan, M. F., Bikun, J., Christiansen, E., Correa, B., Murphy, B., & Self, S. (1980). *Uranium mineralization in fluorine-enriched volcanic rocks*. United States.

Castro, A. (2014). The off-crust origin of granite batholiths. *Geoscience Frontiers, 5*, 63–75.

Castro-Reino, S.F. (2004). *Intrusion-related mineralization in the central sector of the Sierra Madre Oriental*. [Ph.D. thesis]: Mexico, Arizona University.

Centeno-García, E. (2017). Mesozoic tectono-magmatic evolution of Mexico: An overview. *Ore Geology Reviews, 81*, 1035–1052.

Chappell, B. W., Bryant, C. J., Wyborn, D., White, A. J. R., & Williams, I. S. (1998). High- and low-temperature I-type granites. *Resource Geology, 48*, 225–236.

Chappell, B. W., & White, A. J. R. (2001). Two contrasting granite types: 25 years later. *Australian Journal of Earth Sciences, 48*, 489–499.

Chryssoulis, S. L., & Rankin, A. H. (1988). Decrepitometry of fluid inclusions in quartz from the Guadalcazar granite of Mexico; Principles and application to mineral exploration. *Mineralium Deposita, 23*, 42–49.

Chryssoulis, S. L., & Wilkinson, N. (1983). High Silver content of fluid inclusions in quartz from Guadalcazar Granite, San Luis Potosí, Mexico: A contribution to ore-genesis theory. *Economic Geology, 78*, 302–318.

Clemens, J. D., Holloway, J. R., & White, A. J. R. (1986). Origin of an A-type granite: Experimental constraints. *American Mineralogist, 71*, 317–324.

Cuéllar-Cárdenas, M. A., Nieto-Samaniego, Á. F., Levresse, G., Alaniz-Álvarez, S. A., Solari, L., Ortega-Obregón, C., & López-Martínez, M. (2012). Límites temporales de la deformación por acortamiento Laramide en el centro de México. *Revista Mexicana de Ciencias Geológicas, 29*, 179–203.

Dahlquist, J. A., Alasino, P. H., & Bello, C. (2014). Devonian F-rich peraluminous A-type magmatismin the proto-Andean foreland (Sierras Pampeanas, Argentina): Geochemical constraints and petrogenesis fromthewestern-central region of the Achala batholith. *Mineralogy and Petrology, 108*, 391–417.

Dahlquist, J. A., Pankhurst, R. J., Gaschnig, R. M., Rapela, C. W., Casquet, C., Alasino, P. H., Galindo, C., & Baldo, E. G. (2013). Hf and Nd isotopes in early ordovician to early carboniferous granites as monitors of crustal growth in the Proto-Andean margin of Gondwana. *Gondwana Research, 23*, 1617–1630.

Dall'Agnol, R., Frost, C. D., & Rämö, O. T. (2012). IGCP Project 510 "A-type granites and related rocks through time": Project vita, results, and contribution to granite research. *Lithos, 151*, 1–16.

Díaz-Bravo, B. A., Barboza-Gudiño, J. R., Ortega-Obregón, C., & Morales-Gámez, M. (2022). Late Cretaceous to Oligocene overlapping plutonic magmatism episodes in the eastern Mesa Central province of Mexico. *International Geology Review, 64*, 675–697.

Dickinson, W. R., & Gehrels, G. E. (2003). U-Pb ages of detrital zircons from Permian and Jurassic eolian sandstones of the Colorado Plateau, USA: Paleogeographic implications. *Sedimentary Geology, 163*, 29–66.

Eby, G. N. (1992). Chemical subdivision of A-type granitoids: Petrogenetic and tectonic implications. *Geology, 20*, 641–644.

Ferrari, L., Orozco-Esquivel, T., Bryan, S. E., Lopez-Martinez, M., & Silva-Fragoso, A. (2018). Cenozoic magmatism and extension in western Mexico: Linking the Sierra Madre Occidental silicic large igneous province and the Comondú Group with the Gulf of California rift. *Earth-Science Reviews, 183*, 115–152.

Finch, W. I. (1987). *A review of genetic models for major types of uranium deposits in the USA. — Uranium resources and geology of North America*. IAEA-TECDOC-500, Saskatoon, Canada, pp. 81–82.

Foshag, W. F., & Fries, C. (1942). Tin deposits of the Republic of Mexico: US. *Geological Survey Bulletin, 985–C*, 99–176.

Fries, C., & Schmitter, E. (1948). Tin-bearing placers near Guadalcazar, state of San Luis Potosi, Mexico: US. *Geological Survey Bulletin, 990-D*, 109–149.

Frost, B. R., Barnes, C. G., Collins, W. J., Arculus, R. J., Ellis, D. J., & Frost, C. D. (2001). A geochemical classification for granitic rocks. *Journal of Petrology, 42*, 2033–2048.

Frost, C. D., & Frost, B. R. (2011). On ferroan (A-type) granitoids: Their compositional variability and modes of origin. *Journal of Petrology, 52*, 39–53.

Gao, P., Garcia-Arias, M., Chen, Y. X., & Zhao, Z. F. (2020). Origin of peraluminous A-type granites from appropriate sources at moderate to low pressures and high temperatures. *Lithos, 352–353*, 105287.

González-Guzmán, R. (2012). *Origen y Evolución Magmática del Cinturón de Intrusivos de Concepción del Oro [Ph.D. thesis]*. Universidad Autónoma de Nuevo León, Facultad de Ciencias de la Tierra.

Henry, C. D., & Aranda-Gómez, J. J. (1992). The real southern basin and range: Mid-to late Cenozoic extension in Mexico. *Geology, 20*, 701–704.

Huang, H. Q., Li, X. H., Li, W. X., & Li, Z. X. (2011). Formation of high $\delta^{18}O$ fayalite-bearing A-type granite by high-temperature melting of granulitic metasedimentary rocks, southern China. *Geology, 39*, 903–906.

Huerta-González, R.M. (2017). El emplazamiento de pórfidos eocénicos y su posible relación con zonas mineralizadas en la Sierra de Catorce, SLP [Ph.D. thesis]: Universidad Autónoma de San Luis Potosí, México.

Kemp, A. I. S., & Hawkesworth, C. J. (2003). Granitic perspective on the generation and 1120 secular evolution of continental crust. *Treatise on Geochemistry, 3*, 349–410.

King, P. L., Chappell, B. W., Allen, C. M., & White, A. J. R. (2001). Are A-type granites the high-temperature felsic granites? Evidence from fractionated granites of the Wangrah Suite. *Australian Journal of Earth Sciences, 48*, 501–514.

Labarthe-Hernández, G., & Jiménez-López, L. S. (1992). Características físicas y estructura de lavas e ignimbrita riolíticas en la Sierra de San Miguelito S.L.P. *Universidad Autónoma de San Luis Potosí, Instituto de Geología. Folleto Técnico, 114*, 1–34.

Labarthe-Hernández, G., Tristán, M., & Aranda-Gómez, J. J. (1982). Revisión estratigráfica del Cenozoico de la parte central del Estado de San Luis Potosí. *Universidad Autónoma de San Luis Potosí, Instituto de Geología y Metalurgia, Folleto Técnico, 85*, 208.

Le Bas, M., LeMaitre, R. W., Streckeisen, A., & Zanettin, B. (1986). A chemical classification of volcanic rocks base on the total alkali-silica diagram. *Journal of Petrology, 27*, 745–750.

Le Maitre, R. W., Streckeisen, A., Zanettin, B., Le Bas, M. J., Bonin, B., Bateman, P., Bellieni, G., Dudek, A., Efremova, S., Keller, J., Lameyre, J., Sabine, P. A., Schmid, R., Sorensen, H., & Woolley, A. R. (2002). *Igneous rocks: a classification and glossary of terms* (p. 252). Cambridge: Cambridge University Press.

Loiselle, M. C., & Wones, D. R. (1979). Characteristics and origin of anorogenic granites. *Geological Society of America Abstract Program, 11*, 468.

Ludwig, K. R. (2012). User's Manual for Isoplot 3.75: A geochronological toolkit for microsoft excel. Berkeley Geochronology Center, Speical Publication No. 5

Martin, R. F. (2006). A-type granites of crustal origin ultimately result from open-system fenitization-type reactions in an extensional environment. *Lithos, 91*, 125–136.

Mascuñano, E., Levresse, G., López, E. C., Cambra, J. T., Esquivel, R. C., & Meyzen, C. (2013). Post-Laramide, Eocene magmatic activity in Sierra de Catorce, San Luis Potosí, México. *Revista Mexicana de Ciencias Geológicas, 30*, 299–311.

McDonough, W. F., & Sun, S. S. (1995). The composition of the Earth. *Chemical Geology, 120*, 223–253.

Morales Cámera, M. M., Dahlquist, J. A., Basei, M. A. S., Galindo, C., da Costa, C. N. M., & Facetti, N. (2017). F-rich strongly peraluminous A-type magmatism in the pre-Andean foreland Sierras Pampeanas, Argentina: Geochemical, geochronological, isotopic constraints and petrogenesis. *Lithos, 277*, 210–227.

Morales Cámera, M. M., Dahlquist, J. A., Garcia-Arias, M., Moreno, J. A., Galindo, C., Basei, M. A. S., & Molina, J. F. (2020). Petrogenesis of the F-rich peraluminous A-type granites: An example from the Devonian Achala batholith (Characato Suite). *Sierras Pampeanas. Argentina. Lithos, 378–379*, 105792.

Morales Cámera, M. M., Dahlquist, J. A., Ramacciotti, C. D., Galindo, C., Basei, M. A., Zandomeni, P. S., & Grande, M. M. (2018). The strongly peraluminous A-type granites of the Characato suite (Achala batholith), Sierras Pampeanas, Argentina: Evidence of Devonian-Carboniferous crustal reworking. *Journal of South American Earth Sciences, 88*, 551–567.

Moreno, J. A., Baldim, M. R., Semprich, J., Oliveira, E. P., Verma, S. K., & Teixeira, W. (2017). Geochronological and geochemical evidences for extension-related Neoarchean granitoids in the southern São Francisco Craton, Brazil. *Precambrian Research, 294*, 322–343.

Moreno, J. A., Molina, J. F., Bea, F., Anbar, M. A., & Montero, P. (2016). Th-REE and Nb-Ta accessory minerals in post-collisional Ediacaran felsic rocks from the Katernia Ring Complex (S. Sinai, Egypt): An assessment for the fractionation of Y/Nb, Th/Nb, La/Nb and Ce/Pb in highly evolved A-type granites. *Lithos, 258–259*, 173–196.

Moreno, J. A., Molina, J. F., Montero, P., Anbar, M. A., Scarrowa, J. H., Cambeses, A., & Bea, F. (2014). Unraveling sources of A-type magmas in juvenile continental crust: Constraints from compositionally diverse Ediacaran post-collisional granitoids in the Katerina Ring Complex, southern Sinai. *Egypt. Lithos, 192–195*, 56–85.

Nieto-Samaniego, A. F., Alaniz-Álvarez, S. A., & Camprubí, A. (2007). Mesa Central of México: Stratigraphy, structure, and cenozoic tectonic evolution. In S. A. Alaniz-Álvarez & Á. F. Nieto-Samaniego (Eds.), *Geology of México: Celebrating the centenary of the geological society of México* (Vol. 422, pp. 41–70). Geological Society of America Special Paper.

Nieto-Samaniego, Á. F., Alaniz-Álvarez, S. A., & Camprubí Cano, A. (2005). La Mesa Central de México: Estratigrafía, estructura y evolución tectónica cenozoica. *Boletín De La Sociedad Geológica Mexicana, 57*, 285–318.

Nieto-Samaniego, A. F., Alaniz-Alvarez, S. A., & Labarthe-Hernández, G. (1997). La deformación cenozoica poslaramídica en la parte meridionalde la Mesa Central, México. *Revista Mexicana de Ciencias Geológicas, 14*, 13–25.

Nieto-Samaniego, Á. F., Ferrari, L., Alaniz-Alvarez, S. A., Labarthe-Hernández, G., & Rosas-Elguera, J. (1999). Variation of Cenozoic extension and volcanism across the southern Sierra Madre Occidental volcanic province, Mexico. *Geological Society of America Bulletin, 111*, 347–363.

Nieto-Samaniego, A. F., Olmos-Moya, M. D. J. P., Levresse, G., Alaniz-Alvarez, S. A., Abdullin, F., Del Piar-Martínez, A., & Xu, S. (2020). Thermochronology and exhumation rates of granitic intrusions at Mesa Central, Mexico. *International Geology Review, 62*, 311–319.

Orozco-Esquivel, M. T., Nieto-Samaniego, Á. F., & Alaniz-Álvarez, S. A. (2002). Origin of rhyolitic lavas in the Mesa Central, Mexico, by crustal melting related to extension. *Journal of Volcanology and Geothermal Research, 188*, 37–56.

Patiño Douce, A. E. (1997). Generation of metaluminous A-type granitoids by low-pressure melting of calc-alkaline granitoids. *Geology, 25*, 743–746.

Paton, C., Woodhead, J. D., Hellstrom, J. C., Hergt, J. M., Greig, A., & Maas, R. (2010). Improved laser ablation U-Pb zircon geochronology through robust downhole fractionation correction. *Geochemistry, Geophysics, Geosystems*, 11

Pinto-Linares, P. J., Levresse, G., Tritlla, J., Valencia, V. A., Torres-Aguilera, J. M., González, M., & Estrada, D. (2008). Magmas transicionales del tipo adakítico a calcialcalino en un ambiente continental extensivo en los depósitos de Au-Cu de tipo skarn de La Paz, Mesa Central, México: Implicaciones metalogenéticas. *Revista Mexicana de Ciencias Geológicas, 25*, 39–58.

Rodríguez-Ríos, R., & Torres-Aguilera, J. (2009). Evolución petrológica y geoquímica del vulcanismo bimodal oligocénico en el campo volcánico de San Luis Potosí (México). *Revista Mexicana De Ciencias Geológicas, 26*, 658–673.

Rudnick, R. L., & Gao, S. (2003). The composition of the continental crust. In H. D. Holland & K. K. Turekian (Eds.), *Treatise on geochemistry* (pp. 1–64). Oxford: The Crust Elsevier-Pergamon.

Ruiz-Mendoza, V., Verma, S. K., Torres-Sánchez, D., Barry, T. L., Moreno, J. A., & Torres-Hernández, J. R. (2021). Geochemistry and geochronology of intermediate volcanic rocks from the compostela area, Nayarit, Mexico: Implications for petrogenesis and tectonic setting. *Geological Journal, 56*, 4401–4428.

Salas, G. (1975). Carta y provincias metalogenéticas de la República Mexicana, México. *Consejo de Recursos Minerales Bulletin, 21E*, 242.

Siesgesmund, S., López-Doncel, R., Sieck, P., Wilke, H., Wemmer, K., Frei, D., & Oriolo, S. (2018). Geochronological and geochemical constraints on the genesis of Cu-Au skarndeposits of the Santa María de la Paz district (Sierra del Fraile, Mexico). *Ore Geology Reviews, 94*, 310–325.

Silva-Romo, G. (1996). Estudio de la estratigrafía y estructuras tectónicas de la Sierra de Salinas, Estados de SLP y Zacatecas [Ph.D. thesis]: Universidad Nacional Autónoma de México, Facultad de Ciencias.

Singh, P. K., Verma, S. K., Singh, V. K., Moreno, J. A., Oliveira, E. P., & Mehta, P. (2019). Geochemistry and petrogenesis of sanukitoid and high-K anatectic granites from the Bundelkhand Craton, India: Implications for late-Archean crustal evolution. *Journal of Asian Earth Sciences, 174*, 263–282.

Singh, P. K., Verma, S. K., Singh, V. K., Moreno, J. A., Oliveira, E. P., Hua, L. X., Malviya, V. P., & Prakash, D. (2021). Geochronology and petrogenesis of the TTG gneisses and granitoids from the Central Bundelkhand granite-greenstone terrane, Bundelkhand Craton, India: Implications for Archean crustal evolution and cratonization. *Precambrian Research, 359*, 106210.

Stepanov, A. S., Hermann, J., Rubatto, D., & Rapp, R. P. (2012). Experimental study of monazite/melt partitioning with implications for the REE, Th and U geochemistry of crustal rocks. *Chemical Geology, 300–301*, 200–220.

Torres-Hernández, J. R., Labarthe-Hernández, G., Aguillón-Robles, A., Gómez-Anguiano, M., & Mata-Segura, J. L. (2006). The pyroclastic dikes of the Tertiary San Luis Potosi volcanic field: Implications on the emplacement of Panalillo ignimbrite. *Geofisica Internacional, 45*, 243–253.

Torres-Jurado, E. (2019). Análisis geoquímico, petrográfico y estructural de los intrusivos de Guadalcázar y su relación con los yacimientos minerales tipo greisen-skarn. [under graduated thesis]: Universidad Autónoma de San Luis Potosí.

Torres-Sánchez, D., Verma, S. K., Verma, S. P., Velasco-Tapia, F., & Torres-Hernández, J. R. (2019). Petrogenetic and tectonic implications of Oligocene-Miocene volcanic rocks from the Sierra de San Miguelito complex, central Mexico. *Journal of South American Earth Sciences, 95*, 102311.

Torres-Sánchez, D., Verma, S. K., Barry, T. L., Verma, S. P., & Torres-Hernández, J. R. (2020). $^{40}Ar/^{39}Ar$ geocrhonology and petrogenesis of the Sierra de San Miguelito Volcanic Complex, Mesa Central. *Mexico. Lithos, 370–371*, 105613.

Tristán-González, M., Aguillón-Robles, A., Barboza-Gudiño, J. R., Torres-Hernández, J. R., Bellon, H., López-Doncel, R., Rodríguez-Ríos, R., & Labarthe-Hernández, G. (2009). Geocronología y distribución espacial del vulcanismo en el Campo Volcánico de San Luis Potosí. *Boletín de la Sociedad Geológica Mexicana, 61*, 287–303.

Tristán-González, M., Aguillón-Robles, A., Barboza-Gudiño, J. R., Cruz-Márquez, J., García-Arreola, M. E., Bellon, H., & Labarthe-Hernández, G. (2015). Características geoquímicas y significado tectónico del complejo de diques y domos félsicos del Paleoceno-Eoceno de La Tesorera, Zacatecas, en la Mesa Central, México. *Revista Mexicana de Ciencias Geológicas, 32*, 455–474.

Troll, V. R., Sachs, P. M., Schmincke, H. U., & Sumita, M. (2003). The REE–Ti mineral chevkinite in comenditic magmas fromGran Canaria, Spain: A SYXRF-probe study. *Contributions to Mineralogy and Petrology, 145*, 730–741.

Tuta, Z. H., Sutter, J. F., Kesler, S. E., & Ruiz, J. (1988). Geochronology of mercury, tin, and fluorite mineralization in northern Mexico. *Economic Geology, 83*, 1931–1942.

Velasco-Tapia, F., González-Guzmán, R., Chávez-Cabello, G., Lozano-Serna, J., & Valencia-Moreno, M. (2011). Estudio petrográfico y geoquímico del Complejo Plutónico El Peñuelo (Cinturón de Intrusivos de Concepción del Oro), noreste de México. *Boletín de la Sociedad Geológica Mexicana, 63*, 183–199.

Verma, S. P. (2010). Statistical evaluation of bivariate, ternary and discriminant function tectonomagmatic discrimination diagrams. *Turkish Journal of Earth Sciences, 19*, 185–238.

Verma, S. P. (2015). Present state of knowledge and new geochemical constraints on the central part of the Mexican Volcanic Belt and comparison with the Central American Volcanic Arc in terms of near and far trench magmas. *Turkish Journal of Earth Sciences, 24*, 399–1460.

Verma, S. K. (2017). Precambrian plate tectonic setting of Africa from multidimensional discrimination diagrams. *Journal of African Earth Sciences, 125*, 137–150.

Verma, S. P. (2020). *Road from geochemistry to geochemometrics*. Springer.

Verma, S. K., Acosta Fimbres, K. G., Torres-Sánchez, D., Torres-Hernández, J. R., Torres-Sánchez, S. A., & López-Loera, H. (2020). Geochemistry and petrogenesis of Oligocene felsic volcanic rocks from the Pinos Volcanic Complex, Mesa Central, Mexico. *Journal of South American Earth Sciences, 102*, 102704.

Verma, S. K., Pandarinath, K., & Verma, S. P. (2012). Statistical evaluation of tectonomagmatic discrimination diagrams for granitic rocks and proposal of new discriminant-function-based multidimensional diagrams for acid rocks. *International Geology Review, 54*, 325–347.

Verma, S. P., Pandarinath, K., Verma, S. K., & Agrawal, S. (2013). Fifteen new discriminant function- based multi-dimensional robust diagrams for acid rocks and their application to precambrian rocks. *Lithos, 168–169*, 113–123.

Verma, S. P., & Rivera-Gómez, M. A. (2013). Computer programs for the classification and nomenclature of igneous rocks. *Episodes, 36*, 115–124.

Verma, S. P., Rosales-Rivera, M., Rivera-Gómez, M. A., & Verma, S. K. (2019). Comparison of matrix-effect corrections for ordinary and uncertainty weighted linear regressions and determination of major element mean concentrations and total uncertainties of sixty-two international geochemical reference materials from wavelength-dispersive X-ray fluorescence spectrometry. *Spectrochimica Acta Part B, 162*, 105714.

Verma, S. K., Torres-Sánchez, D., Hernández-Martínez, K. R., Malviya, V. P., Singh, P. K., Torres-Hernández, J. R., & Rivera-Escoto, B. A. (2021). Geochemistry of Eocene felsic volcanic rocks from the Mesa Virgen-Calerilla, Zacatecas, Mexico: Implications for the magma source and tectonic setting. *Geological Journal, 56*, 3771–3790.

Verma, S. K., Verma, S. P., Oliveira, E. P., Singh, V. K., & Moreno, J. A. (2016). LA-SF-ICP-MS zircon U-Pb geochronology of granitic rocks from the central Bundelkhand greenstone complex, Bundelkhand craton, India. *Journal of Asian Earth Sciences, 118*, 125–137.

Verma, S. P., Verma, S. K., Rivera-Gómez, M. A., Torres-Sánchez, D., Díaz-González, L., Amezcua-Valdez, A., & Pandarinath, K. (2018). Statistically coherent calibration of X-ray fluorescence spectrometry for major elements in rocks and minerals. *Journal of Spectroscopy, 2018*, 1–13.

Watson, E. B., & Harrison, T. M. (1983). Zircon saturation revisited: Temperature and composition effects in a variety of crustal magma types. *Earth and Planetary Science Letters, 64*, 295–304.

Whalen, J. B., Currie, K. L., & Chappell, B. W. (1987). A-type granites: Geochemical characteristics, discrimination and petrogenesis. *Contributions to Mineralogy and Petrology, 95*, 407–419.

Wiedenbeck, M. A. P. C., Alle, P., Corfu, F., Griffin, W. L., Meier, M., Oberli, F. V., & Spiegel, W. (1995). Three natural zircon standards for U-Th-Pb, Lu-Hf, trace element and REE analyses. *Geostandards Newsletter, 19*, 1–23.